Zircon and titanite U-Pb dating of the Zhangjiawa iron skarn deposit, Luxi district, North China Craton: Implications for a craton-wide iron skarn mineralization

Zhuang Duan [a], Jian-Wei Li [a,b,*]

[a] Faculty of Earth Resources, China University of Geosciences, Wuhan 430074, China
[b] State Key Laboratory of Geological Processes and Mineral Resources, China University of Geosciences, Wuhan 430074, China

ARTICLE INFO

ABSTRACT

The North China craton hosts numerous iron skarn deposits containing more than 2600 Mt of iron ores, mostly with an average grade of >45 wt% Fe, which have been among the most important source of high-grade iron ores for the last three decades in China. These deposits typically form clusters and can be roughly divided into the western and eastern belts, which are located in the middle of Trans-North China orogen and to the west of the Tan-Lu fault zone in the eastern part of North China craton, respectively. The western belt mainly consists of the southern Taihang district, as well as the Linfen and Taiyuan ore fields, whereas the eastern belt comprises the Luxi and Xu-Huai districts. The Zhangjiawa deposit in the Luxi district has proven reserves of 290 Mt at an average of 46% Fe (up to >65%). The iron mineralization occurs mainly along contact zones between the Kuangshan dioritic intrusion and middle Ordovician marine carbonate rocks that host numerous evaporite intercalations. Titanite grains from the mineralized skarn are closely intergrown with magnetite and retrograde skarn minerals including chlorite, phlogopite and minor epidote, indicating a hydrothermal origin. The titanite grains have extremely low REE contents and low Th/U ratios, consistent with their precipitation directly from hydrothermal fluids responsible for the iron mineralization. Ten hydrothermal titanite grains yield a weighted mean $^{206}Pb/^{238}U$ age of 131.0 ± 3.9 Ma (MSWD = 0.1, 1σ), which is in excellent agreement with a zircon U-Pb age (130 ± 1 Ma) of the ore-related diorite. This age consistency confirms that the iron skarn mineralization is temporally and likely genetically related to the Kuangshan intrusion. Results from this study, when combined with existing isotopic age data, suggest that iron skarn mineralization and associated magmatism throughout both the eastern and western belts took place coevally between 135 and 125 Ma, with a peak at ca. 130 Ma. As such, those deposits may represent the world's only major Phanerozoic iron skarn concentration hosted in Precambrian cratons. The magmatism and associated iron skarn mineralization coincide temporally with the culmination of lithospheric thinning and destruction of the North China craton, implying a causal link between the two.

© 2017 Elsevier B.V. All rights reserved.

1. Introduction

Cratons are well endowed with a large variety of ore deposits that were generally emplaced during craton formation. However, few endogenic ore deposits have been generated after the formation or stabilization of a cratonic block (Groves and Bierlein, 2007). The North China craton (NCC) is an extraordinary exception to this guideline because it experienced large-scale magmatism and strong internal extensional deformation in the late Mesozoic,

having been interpreted as a result of significant removal of the lithospheric keel of the craton (Griffin et al., 1998; Menzies and Xu, 1998; Zhu et al., 2011). The associated magmatic activities and structural processes produced numerous Fe, Au, Mo and Ag-Pb-Zn deposits (e.g., Yang et al., 2003; Li et al., 2012, 2013b; Li and Santosh 2014; Zhu et al., 2015). Of these deposit types, the iron skarn deposits in the NCC have provided a significant source of high-grade iron ores, with total proven reserves of >2600 Mt at an average grade of >45% (Yao et al., 1993; Zhang et al., 2014b).

Iron skarn deposits of the NCC cluster in several major districts, forming two roughly NNE-striking belts in the central-eastern NCC (Fig. 1). The eastern belt consists of the Luxi and Xu-Huai districts to the west of the Tan-Lu fault zone, whereas the western belt
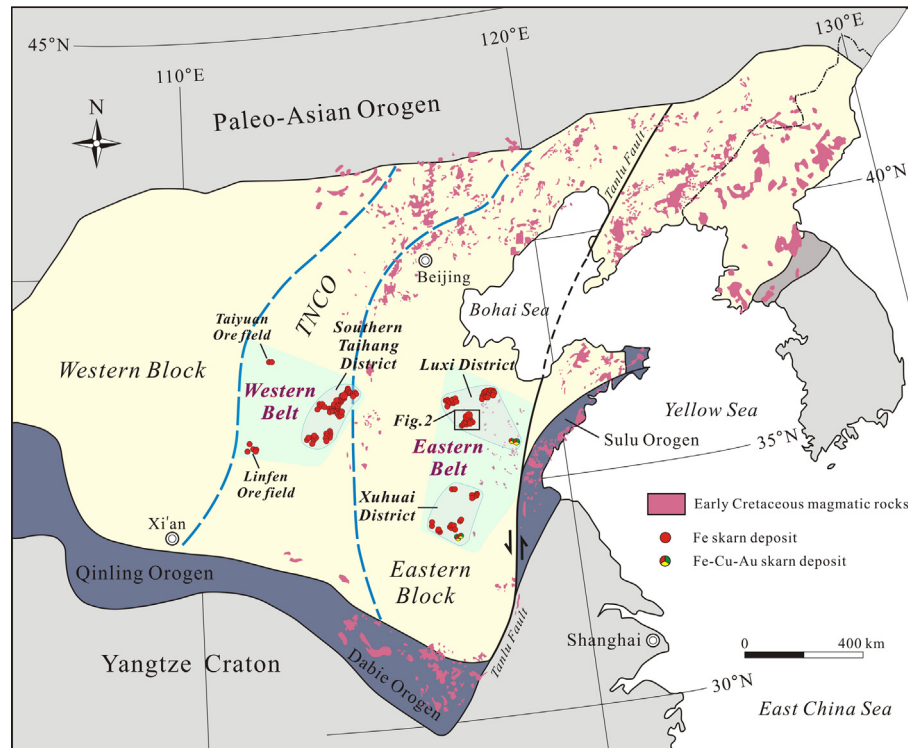
Fig. 1. Map of the North China Craton (NCC) and distribution of major iron skarn deposits in several districts (modified from Zhu et al., 2015). TNCO = Trans-North China orogen.

comprises the Southern Taihang district, as well as the Linfen and Taiyuan ore fields within the Trans-North China orogen that separates the Western block of the NCC from the Eastern block (Zhao et al., 2005). All these iron districts are characterized by widespread evaporites within the middle-lower Ordovician marine carbonates into which the ore-related intrusions were emplaced. Previous $^{40}Ar/^{39}Ar$ and U-Pb geochronological studies have constrained the ore formation within the Handan-Xingtai ore field in the western belt to a period between 137 and 129 Ma (Zheng et al., 2007; Shen et al., 2013; Deng et al., 2014, 2015b). However, robust age data are scarce for iron skarn deposits of the Luxi district from the eastern belt, leaving open question whether iron skarn mineralization in the western and eastern belts occurred coevally or separately. The Zhangjiawa deposit represents the largest iron skarn deposit in the Luxi district, with proven reserves of ~290 Mt at an average of ~46% (Zong et al., 2012). In this paper, we present U-Pb dating results of hydrothermal titanite from iron ores of the Zhangjiawa deposit and values of magmatic zircon from the ore-related intrusion to precisely constrain the time of magmatism and iron skarn mineralization in the district. The results, when combined with previously published age data in other iron skarn districts, allow us to unravel the chronological framework of iron skarn deposits over the NCC, which in turn, points to a genetic link between pervasive iron skarn mineralization and tectonic reactivation or decratonization of the NCC.

2. Geological background

The North China craton (NCC) was stablized at ca. 1.85 Ga by amalgamation of the Western and Eastern blocks along the Trans-North China orogen (Fig. 1; Zhao et al., 2001). The basement of the NCC is dominated by Archean to Paleoproterozoic TTG gneiss, granite, charnockite, migmatite, amphibolite, greenschist, pelitic schist, Al-rich gneiss, banded iron formations, calc-silicate

rocks and marble, all of which are unconformably overlain by Mesoproterozoic unmetamorphosed volcanic-sedimentary successions (Zhao et al., 2005) and late Paleoproterozoic to late Paleozoic shallow-marine carbonate platform sedimentary rocks (Yang et al., 1986). After a long period of stability, the entire Eastern block and the Trans-North China orogen were significantly reactivated in the late Mesozoic (Zhu et al., 2012b), as indicated by voluminous magmatism, widespread rift-basin development and emplacement of numerous metamorphic core complexes (Liu et al., 2005; Wang et al., 2011b; Charles et al., 2012).

The Luxi district in the eastern NCC is bounded on the east by the translithospheric Tan-Lu Fault (Fig. 1; Chen et al., 2008b; Zhu et al., 2002, 2003). Lithologically, this district comprises Neoarchean gneisses, amphibolites and TTGs, Paleoproterozoic granitoids, Paleozoic carbonates interbedded with clastic rocks, and Mesozoic continental clastic and volcaniclastic rocks. These rocks are variably intruded by late Mesozoic plutons ranging in composition from gabbro to granite.

The Laiwu ore field in the central part of the Luxi district (Fig. 1) hosts a major proportion of the iron skarn ores in the eastern belt. Lithologically it is dominated by amphibolite-facies metamorphic rocks of the Archean Taishan Group, early Paleozoic (Cambrian to middle Orodovician) marine carbonate sequences and late Paleozoic (Carboniferous and Permian) coal-bearing, clastic rocks. The Jurassic to Cenozoic continental sedimentary and volcanic rocks are locally distributed in the eastern half of the district. The Cambrian sequences consist of red sandstones, shales, limestones, and dolomitic limestones, with a total thickness ranging from 562 to 1111 m. The 363–1278-m-thick Ordovician strata, conformably overlying the upper Cambrian limestones, consist mainly of limestones and dolomites with numerous interbeds of gypsum, individually up to 160 m thick (Tang, 1996). The lower Ordovician sequence is divided into the Zhifangzhuang, Donghuangshan, Beianzhuang, Tuyu and Wuyang Formations (Fms.), whereas the middle Ordovician rocks are represented by the Gezhuang and

Badou Fms., which host large iron skarn deposits in the Laiwu ore field (Zeng et al. 1998). Carboniferous and Permian shales, mudstones, sandstones and coal beds, with a total thickness of 245–380 m, unconformably overlie the Ordovician strata and are distributed mainly in the central part of the district. The Cenozoic Laiwu fault basin, which is about 70 km long and 8–22 km wide, is bounded by the Shimen'guanzhuang-Quanli Fault to the south and two arcuate faults (the Taian-Caizhuang and Taian-Xiaoyi faults) to the north (Fig. 2).

The Paleozoic sedimentary rocks are intruded by four major plutons, which range in composition from gabbro to diorite and monzonite, including the Kuangshan, Jiaoyu, Jinniushan and Tietonggou intrusions (Fig. 2). The Kuangshan pluton is the most important ore-related intrusion in the Laiwu ore field, with 13 iron skarn deposits being developed along contact zone between the pluton and the Ordovician carbonates. These deposits combined have proven reserves of ~500 Mt iron ore with average grades of 41–56% (Zong et al. 2010, 2012). In contrast, no economic iron skarn deposits have been found associated with the other three plutons. Zircon U-Pb geochronological studies have revealed that the Jiaoyu and Tietonggou dioritic plutons were emplaced at 130–135 Ma (Yang et al., 2006; Xu et al., 2004b; Lan et al., 2013). These early Cretaceous magmatic rocks are interpreted to have formed from mixing of lower crustal and enriched lithospheric mantle-derived magmas (Chen et al., 2013; Lan et al., 2013).

3. Geology and mineralization of the Zhangjiawa deposit

3.1. Deposit geology

The Zhangjiawa deposit is located in the northern contact zone between the Kuangshan diorite pluton and the middle Ordovician Gezhuang and Badou Fms., which consist of evaporite-bearing and dolomitic limestones (Zong et al., 2012). These limestones are unconformably overlain by the Carboniferous Benxi and Taiyuan Fms., which are dominated by sandstones, sandy shales, and coal-beds. The Paleozoic sedimentary rocks are unconformably overlain by the widespread Tertiary Guanzhuang Group consisting of conglomerates, siltstones and sandstones. The basal layers of the Guanzhuang Group consist of conglomerate and contain abundant gravels of hematite ore, which are interrpeted as a product of oxidation of primary magnetite orebodies followed by erosion during the uplift that formed the Cenozoic fault basin.

The Kuangshan pluton, with an exposed area of ~9 km², intrudes the Paleozoic rocks along the SW-SN-trending axial trace of the Kuangshan anticline. It consists of pyroxene diorite, biotite-pyroxene-bearing diorite, syenodiorite and porphyritic diorite with no obvious internal intrusive contacts, indicating successive emplacement of different magmas over a short period of time presumably evolved from the same parental magma chamber (Meng, 1988). The biotite-pyroxene-bearing diorite is the most volumetrically important and is composed predominantly of plagioclase (55–65 vol.%) and hornblende (20–30 vol.%), with minor amounts of biotite (~5 vol.%) and pyroxene (3–5 vol.%), with accessory zircon, magnetite, titanite and apatite.

3.2. Mineralization and alteration

The Zhangjiawa iron skarn deposit consists of three mining areas (mines), including Zhangjiawa, Gangli and Xiaoguanzhuang, with the former two being separated by the F_1 fault (Fig. 3A). Mineralization is mainly localized along the northern contact between the Kuangshan pluton and the evaporite-bearing and dolomitic limestones of the middle Ordovician Badou Fm., with lesser amounts of iron ore being hosted in fracture zones overprinting the unconformity between the Carboniferous Benxi Fm. and middle Ordovician Badou Fm. Within ~1000 m of the Kuangshan pluton, the Paleozoic carbonate and shale sequences have been thermally metamorphosed to marbles and hornfels. The marbles adjacent to the intrusion have been intensely deformed into composite folds with ductile flow fabrics, and overprinted by magnesium skarn assemblages dominated by spinel, forsterite, diopside and serpentine. Throughout the three mining areas, diopside skarns are developed only locally in the footwall of most iron orebodies, whereas serpentine-chlorite skarns are commonly interbedded with thin orebodies.

The Zhangjiawa mine (47 Mt @ 47% Fe) consists of ten orebodies that are localized along intrusive contacts between the diorite and
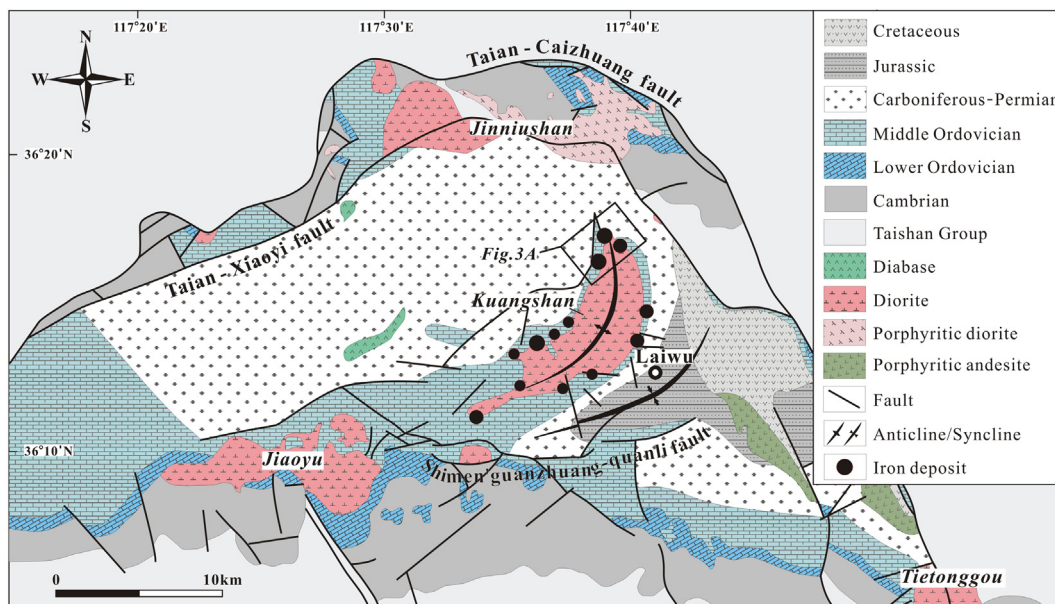

Fig. 2. Geological map of the Laiwu ore field showing the iron skarn deposits controlled by the Kuangshan intrusion (modified after Zong, 1978). The Cenozoic strata in this field are not shown.
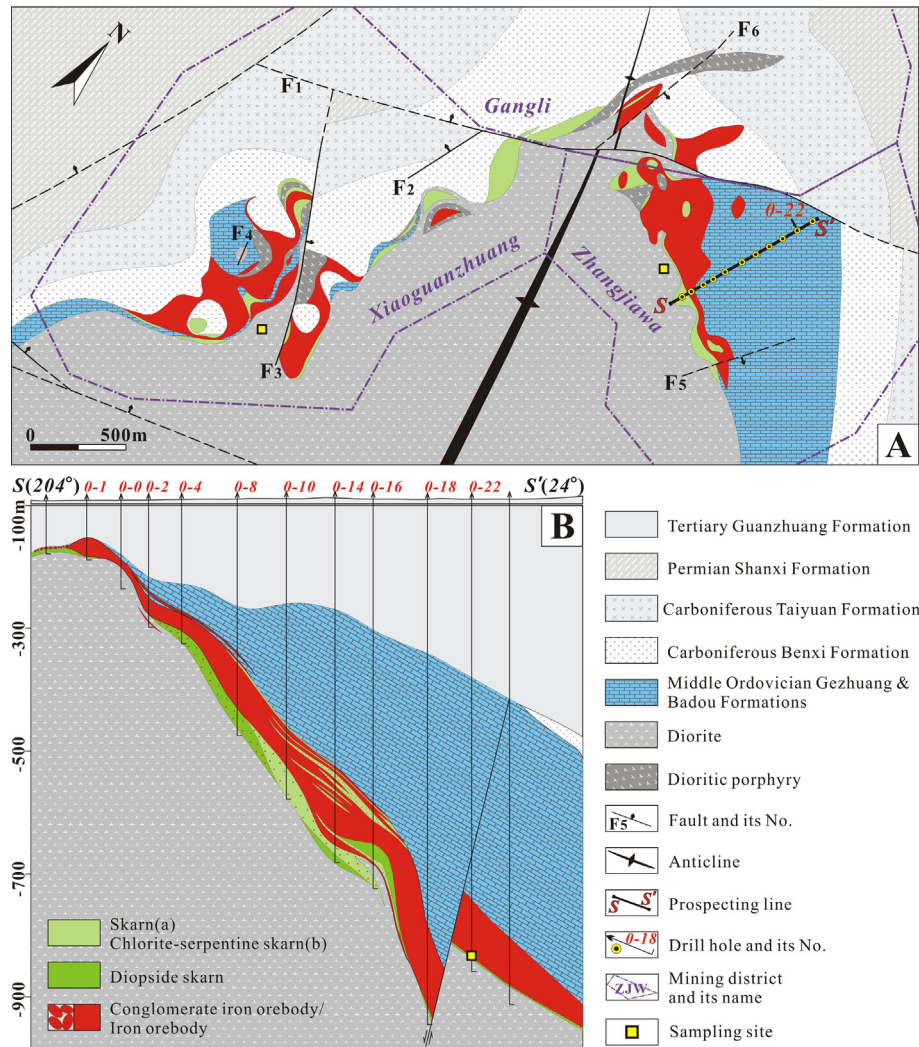
Fig. 3. Geological map (A) and S-S′ cross section (B) of the Zhangjiawa iron skarn deposit including the three mining areas of Zhangjiawa, Xiaoguanzhuang and Gangli, and showing the occurrence of iron orebodies and associated skarns. Also shown are sampling sites for the mineralized skarn and ore-related diorite.

middle Ordovician carbonates. Individual orebody extends for 1000–1200 m in a NW direction and dip 20–50° to northeast. The main orebody, accounting for 98% of the total iron reserves of the deposit, has a vertical extent of 750 m between −150 to −900 m below the present surface. It is lenticular or stratiform in morphology and is 1200 m long, 1100 m wide, and 10 to 30 m thick. Post-ore normal faulting has offset the main orebody by ~200 m (Fig. 3B). The Xiaoguanzhuang mine (90 Mt @ 46% Fe) consists of eight orebodies that are mainly located along the contacts between the dioritic porphyry and middle Ordovician carbonates but minor ores are hosted in fracture zones developed along the unconformity between the Carboniferous Benxi Fm. and middle Ordovician Badou Fm., locally extending into the serpentinized marbles. Four main orebodies, located between −200 and −570 m below the present surface, are tabular in morphology and dip 10–30° northwest. Individual orebodies are 600–1000 m long, 300–500 m wide, and 10–20 m thick. The Gangli mine (146 Mt @ 45% Fe) comprises four main orebodies that occur between −34 to −875 m below the present surface and are developed along the lithological boundary between the Carboniferous and Ordovician strata at shallow-levels but extend into a steep, intrusive contact zone between the diorite and middle Ordovician carbonate rocks at depth. They typically have lenticular or stratiform

morphology, and are 920–1400 m long, 430–910 m wide, and 14–30 m thick (LMM Corp., 2009; Zong et al., 2010).

Field and textural relationships indicate four hydrothermal paragenetic stages, which are represented by albitization, prograde skarn alteration, retrograde skarn alteration, and sulfide-calcite deposition, respectively. The earliest albitization is extensively developed along the margin of the Kuangshan pluton, where plagioclase and hornblende are commonly replaced by fine-grained albite and scapolite, which typically obliterate the original igneous texture (Fig. 4A, B). The prograde skarns are mainly developed in the endoskarn zone and are commonly a few to more than 10 m in thickness. They consist of >80% diopside, with minor andradite, spinel and forsterite. Such rocks, however, are rarely present in the exoskarn zone or in the massive magnetite ores. The poorly-deveolped retrograde skarn assemblages, in the form of phlogopite, serpentine, chlorite and minor epidote, titanite and apatite, are closely associated with magnetite ores. Magnetite typically occurs as small anhedral to euhedral grains, texturally equilibrated with minor serpentine, phlogopite and titanite (Fig. 4D-F, Fig. 5D-F). Some coarse-grained magnetite contains abundant fine-grained spinel as exsolutions (Fig. 4G). In most cases, the magnetite contains high MgO (5.2–6.6 wt%) and MnO (1.1–1.3 wt%) (Fei et al., 2014), indicating significant influence of the middle Ordovician
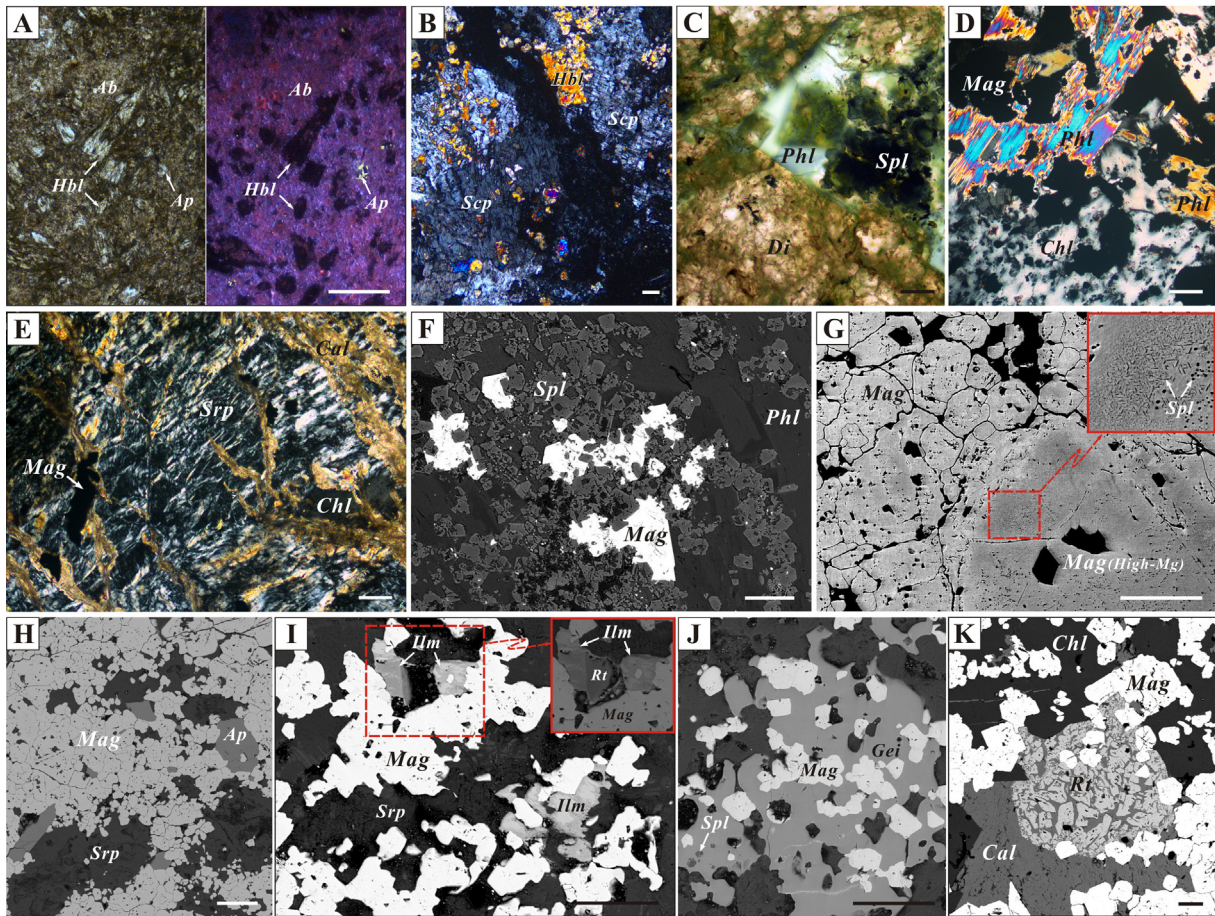
Fig. 4. Photomicrographs (A-E) and BSE image (F-K) showing prograde and retrograde skarn assemblages of the Zhangjiawa iron skarn deposit. (A) Albitization in diorite from Kuangshan intrusion. Plagioclase is replaced by albite (Ab) with indistinct grain boundary revealed in optical cathodoluminescence photomicrograph. (B) Plagioclase and hornblende (Hbl) in diorite is replaced by scapolite (Scp). (C) Spinel (Spl) and phlogopite (Phl) occur as interstitial grains to diopside (Di) aggregates. (D) Phlogopite is associated with magnetite (Mag) and altered by chlorite (Chl). (E) Serpentine (Srp) is overprinted by calcite (Cal) veins and chlorite. (F) Euhedral spinel replaced by magnetite and phlogopite. (G) Fine-grained spinel usually exsolved from coarse-grained magnetite with high-Mg and BSE-dark features. (H) Euhedral apatite grains occur in association with magnetite and serpentine. (I-K) Ti-rich minerals, including ilmenite (Ilm), geikielite (Gei) and rutile (Rt), are closely associated with magnetite, chlorite and serpentine. (Figure scale: 100 μm).

carbonates on the magnetite compositions, presumably by fluid-rock interaction. Minor titanium oxides, including ilmenite, Mn-ilmenite, geikielite and rutile, are intergrown with, or enclosed in magnetite (Fig. 4I-K). The paragenetically latest stage is represented by sulfide-calcite veins and stockworks locally overprinting prograde and/or retrograde skarn assemblages. Sulfide minerals are mainly pyrite, with subordinate chalcopyrite and chalcocite.

Conglomerate-type iron orebodies occur in the Zhangjiawa and Xiaoguanzhuang mines. This type of ores is dominated by supergene hematite that forms discontinuous layers along the basal bed of the Paleogene Guanzhuang Fm., which consists mainly of conglomerate and sandstone (Fig. 3B). Abundant native copper and goethite occur as inclusions, fissure infillings, or stringers in the hematite ores. Field and petrographic data indicate that the conglomerate-type hematite ores formed as a result of weathering of the primary magnetite ores when they were brought to the paleosurface due to tectonic uplift, and subsequently buried by Tertiary sediments.

4. Samples and analytical methods

All samples for in-situ U-Pb dating and trace element analysis were collected from drill cores or underground workings (Fig. 3). Sample 0-22-36 is an iron mineralized endoskarn collected from drill hole ZK0-22 in the Zhangjiawa mine. It consists of diopside (85 vol.%) and minor phlogopite, chlorite, epidote, magnetite and titanite (10 vol.%). This sample was used for in-situ U-Pb dating of hydrothermal iron mineralization. Samples ZJWX-7 and XGZZ-7 were collected from the ore-related diorite in the Zhangjiawa and Xiaoguanzhuang mines, respectively. These two samples were used for zircon U-Pb dating of the intrusive magmatism and as an external standard to test the reliability of the titanite U-Pb dates.

Standard petrographic thin sections were prepared from sample 0-22-36 and used to identify in situ titanite grains for dating. In contrast, zircon grains in the two magmatic samples (ZJWX-7 and XGZZ-7) were separated using conventional heavy liquid and magnetic methods, and then handpicked under a binocular microscope. The grains were then mounted in epoxy mounts and polished to expose their interiors. Both the polished thin sections of the mineralized endoskarn samples and zircon mounts were carbon coated and then studied using back-scattered electron (BSE) and cathodoluminescence (CL) imaging to characterize the morphology and internal structure of the titanite and zircon grains. These analyses were carried out with a FEI Quanta 450 field-emission scanning electron microscope (SEM) equipped with a MonoCL4+ detector at the State Key Laboratory of Geological Processes and Mineral Resources (GPMR), China University of Geosciences, Wuhan.
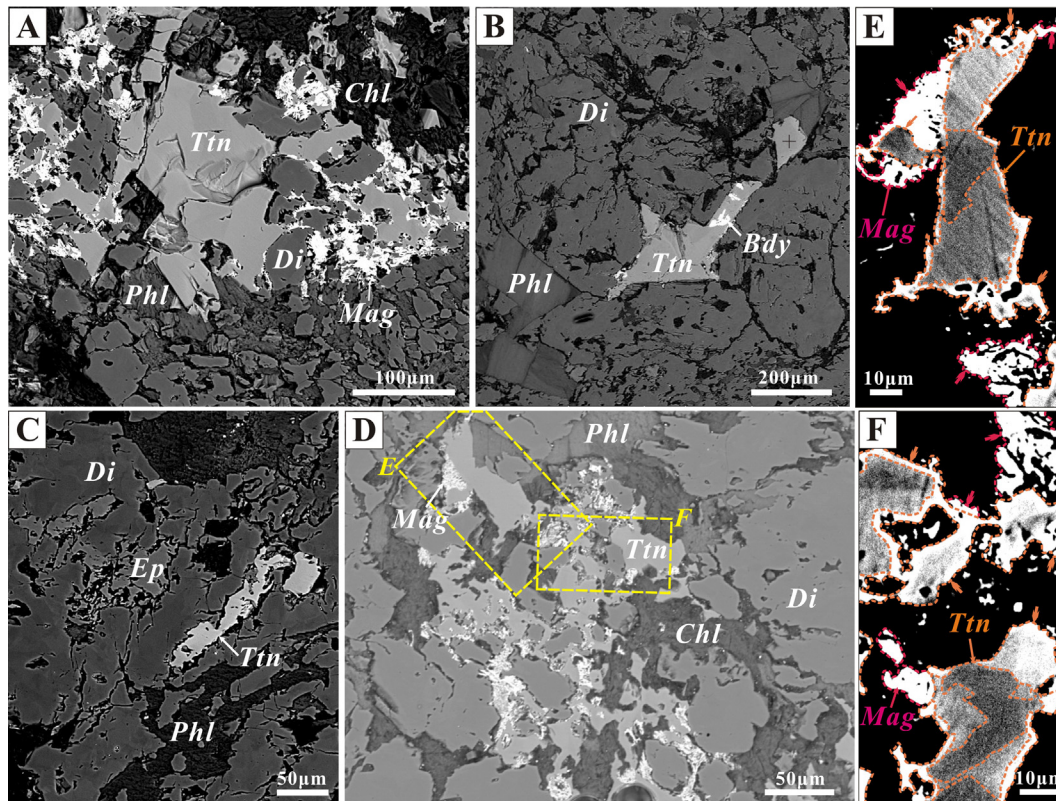
Fig. 5. BSE images showing the occurrences of titanite investigated in this study. (A) Diopside (Di) is overprinted by titanite (Ttn), chlorite (Chl), phlogopite (Phl) and magnetite (Mag). (B) Minor fine-grained baddeleyite (Bdy) occurs enclosed in titanite grains. (C, D) Retrograde skarn minerals, including titanite, chlorite, phlogopite, magnetite and minor epidote (Ep), occur as interstitial assemblages to diopside, or overprint diopside. (E, F) Titanite grains are subhedral to anhedral crystals with obvious irregular zoning, and are typically intergrowth with magnetite.

Trace elements and the U-Th-Pb isotopes of the zircon were analyzed simultaneously by LA-ICP-MS at the State Key Laboratory of GMPR. Laser sampling was performed using a GeoLas 2005, and an Agilent 7500a ICP-MS instrument was used to acquire ion-signal intensities. Detailed operating conditions and data reduction methods are given in Liu et al. (2008, 2010) and are briefly summarized here. A spot size of 32 μm was used for all analyses. Argon was used as the make-up gas and mixed with the carrier gas (helium) via a T-connector before entering the ICP. Nitrogen was added into the central gas flow (Ar + He) of the Ar plasma to improve the detection limit and precision, thus increasing the sensitivity for most elements by a factor 2–3 (Hu et al., 2008). Zircon 91500 was used as a calibration standard for mass discrimination and U-Th-Pb isotope fractionation. Time-dependent drift of U-Th-Pb isotopic ratios was corrected using a linear interpolation (with time) for every five analyses according to the variations of 91500 (Liu et al., 2010). Preferred U-Th-Pb isotopic ratios used for 91,500 are from Wiedenbeck et al. (1995). Trace elements were calibrated against a glass standard (NIST SRM610) combined with internal standardization (Si). Off-line selection and integration of background and analyzed signals, and time-drift correction and quantitative calibration for trace element analyses and U-Pb dating were performed by ICPMSDataCal (Liu et al., 2008, 2010). Uncertainties of preferred values for the external standard 91500 were propagated into the ultimate results of the samples.

Trace elements and U-Pb isotopes of titanite were determined simultaneously using an Agilent 7500a Q-ICP-MS, equipped with a 193 nm excimer laser-ablation system at the Institute of Geology and Geophysics, Chinese Academy of Sciences (IGGCAS) in Beijing. The sample cell was a cylindrical container (ca. 10 cm^3) attached to the Geolas Plus. The detailed analytical techniques were similar to that for zircon and described in Yang et al. (2009) and Sun et al. (2010). Before analysis, the Pulse/Analogy (P/A) factor of the detector was corrected. The instrumental parameters were optimized using a tuning solution in order to make productivity of oxide CeO$^+$/Ce$^+$ and doubly charged species (monitored by Ce^{2+}/Ce$^+$) less than 1% and 3%, respectively, and sensitivity for ^{89}Y better than 2×10^6 cps/ppm. NIST SRM610 standard glass was used to optimize the instrument during laser ablation. Different dwell time was selected, with 15 ms for ^{204}Pb, ^{206}Pb and ^{208}Pb, 30 ms for ^{207}Pb, 10 ms for ^{232}Th and ^{238}U and 6 ms for all others. Each spot analysis consisted of a 30 s background acquisition and 60 s data acquisition and 60 s for cleaning the sample cell and plumbing lines. Each set of 8 analyses was followed by three measurements of the titanite standard (two for BLR-1 and one for OLT-1) and one measurement of NIST SRM 610. The parameters were 40 μm spot size and 6 Hz repetition rate. Trace element concentrations were calibrated using ^{43}Ca as an internal calibration for titanite (CaO weight 28.4% for titanite), with NIST SRM 610 as the reference material. ^{207}Pb/^{206}Pb and ^{206}Pb/^{238}U ratios were calculated using the GLITTER program (GEMOC, Macquarie University; Griffin et al., 2008). After obtaining the Pb isotopic ratios, a common-Pb correction for zircon was applied using the method of Andersen (2002), because the signal intensity of ^{204}Pb was much lower than the other Pb isotopes and there is a large isobaric interference from ^{204}Hg. The measured, uncorrected, compositions of titanite were plotted on a Tera-Wasserburg Concordia diagram (Tera and Wasserburg, 1972), and they define a line which intersects the y-axis at the common ^{207}Pb/^{206}Pb value and shows a lower-intercept age, approximately representing the sample formation

Table 1
Trace element analysis results (ppm) of the Zhangjiawa titanite by LA-ICPMS.

Sample No.	Y	La	Ce	Pr	Nd	Sm	Eu	Gd	Tb	Dy	Ho	Er	Tm	Yb	Lu	Hf	ΣREE	LREE/HREE	Lu/Hf	δEu	δCe
	ppm	ppm	ppm	ppm	ppm	ppm	ppm	ppm	ppm	ppm	ppm	ppm	ppm	ppm	ppm	ppm	ppm				
0-22-36-Hydrothermal titanite																					
0-22-36-1	46.42	0.57	1.84	0.43	3.49	3.06	0.91	4.12	0.99	7.57	1.81	4.68	0.83	5.31	0.50	221.8	36.11	0.40	0.0023	0.78	0.87
0-22-36-2	131.24	5.51	34.80	8.72	62.11	30.91	6.86	36.00	6.94	37.39	5.93	13.09	1.39	7.16	0.61	250.34	257.42	1.37	0.0024	0.63	0.99
0-22-36-3	360.67	22.57	151.33	40.98	270.73	107.87	34.44	105.27	17.72	94.65	15.25	31.95	3.18	18.14	1.33	518.9	915.41	2.18	0.0026	0.98	0.94
0-22-36-4	217.02	9.73	71.00	19.38	136.34	58.61	20.85	58.39	11.17	61.69	10.72	16.76	1.49	11.50	1.04	472.34	488.67	1.83	0.0022	1.08	0.95
0-22-36-5	226.45	6.99	60.83	18.16	117.43	53.53	20.94	62.70	11.31	59.25	10.16	21.01	2.11	12.41	0.74	477.71	457.57	1.55	0.0015	1.10	0.90
0-22-36-6	289.37	8.46	81.14	21.68	154.12	61.84	25.64	72.98	13.94	76.45	13.53	25.72	2.70	12.26	1.01	486.31	571.47	1.61	0.0021	1.16	1.00
0-22-36-7	349.27	20.42	150.32	40.32	247.77	94.73	37.53	95.63	16.55	94.58	14.68	29.84	3.29	16.33	1.52	498.84	863.51	2.17	0.0030	1.19	0.96
0-22-36-8	515.41	35.14	238.49	59.66	358.96	132.33	56.53	128.81	24.18	130.90	22.15	45.06	5.61	26.21	2.28	511.02	1266.31	2.29	0.0045	1.31	1.00
0-22-36-9	238.66	9.04	78.05	23.26	157.04	65.53	26.87	72.48	12.75	69.23	10.51	20.83	2.35	9.65	0.98	604.58	558.57	1.81	0.0016	1.19	0.90
0-22-36-10	101.52	6.03	33.30	8.35	57.58	21.96	4.63	26.54	4.90	30.68	4.41	10.16	0.88	5.58	0.66	248.12	215.66	1.57	0.0027	0.59	0.96
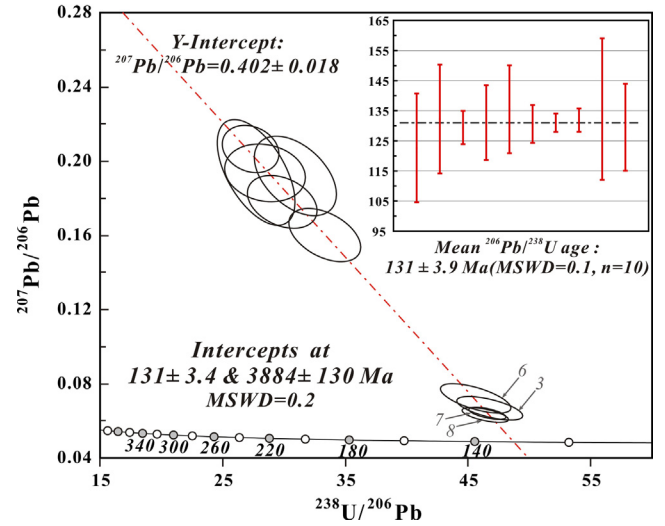
Fig. 6. Tera-Wasserburg and weighted average diagram for the titanite in skarn from the Zhangjiawa deposit.

age. The measured ^{207}Pb was applied for common-Pb correction using the two-stage model of Stacey and Kramers (1975) (see also Williams, 1998). Concordia diagrams and ^{206}Pb/^{238}U weighted mean calculations of zircon and titanite were made using Isoplot/ Ex_ver3 (Ludwig, 2003).

5. Results

5.1. Petrographic features of titanite

Titanite in the mineralized endoskarn sample occurs as anhedral to subhedral grains ranging in diameter from 50 to 200 μm (Fig. 5). These titanites are texturally associated with retrograde skarn minerals including phlogopite, magnetite, chlorite, epidote and allanite (Fig. 5), commonly occurring as interstitial grains between those minerals. Titanite is also closely associated with magnetite (Fig. 5A, D-F). Fine-grained baddeleyite has been locally recognized as inclusions in some titanite grains (Fig. 5B). Most of the titanite grains have a homogeneous texture, but some are zoned and consist of irregular cores and overgrowth domains (Fig. 5E, F).

5.2. Trace element composition and U-Pb age of titanite

Trace element compositions of the titanite are listed in Table 1 and shown in Fig. 9. The titanite grains contain 12–259 ppm U and 0.39–14 ppm Th, with low Th/U ratios of 0.02–0.39. Hafnium and Lu contents range from 222 to 605 ppm and 0.5 to 2.3 ppm, respectively, yielding very low Lu/Hf ratios of 0.0015 to 0.0045. The titanite grains have variable REE concentrations ranging from 36 to 1266 ppm, and are characterized by LREE depletion and low LREE/HREE ratios of 0.4–2.29. Their chondrite-normalized REE patterns generally show weakly positive Eu anomalies (δEu = 0.98–1.31) but no Ce anomalies (δCe = 0.9–1). However, three titanite grains (spots 1, 2, 10) are distinct in that they have much lower REE contents (36, 257 and 216 ppm) with significantly lower LREE/HREE ratios (0.4, 1.37, and 1.57) than the other grains and negative Eu anomalies (0.78, 0.63, and 0.59).

The U-Pb isotope data for the titanite grains are summarized in Table 2. They define a well-constrained mixing line between radiogenic and common-Pb components on the Tera-Wasserburg dia-
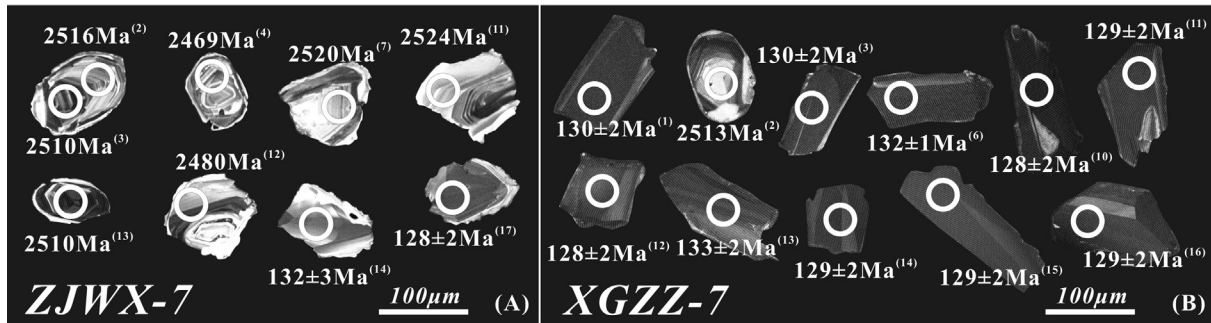
Fig. 7. Cathodoluminescence (CL) images of representative zircon grains with analytical spots and ages (in Ma) from diorite samples ZJWX-7 and XGZZ-7.
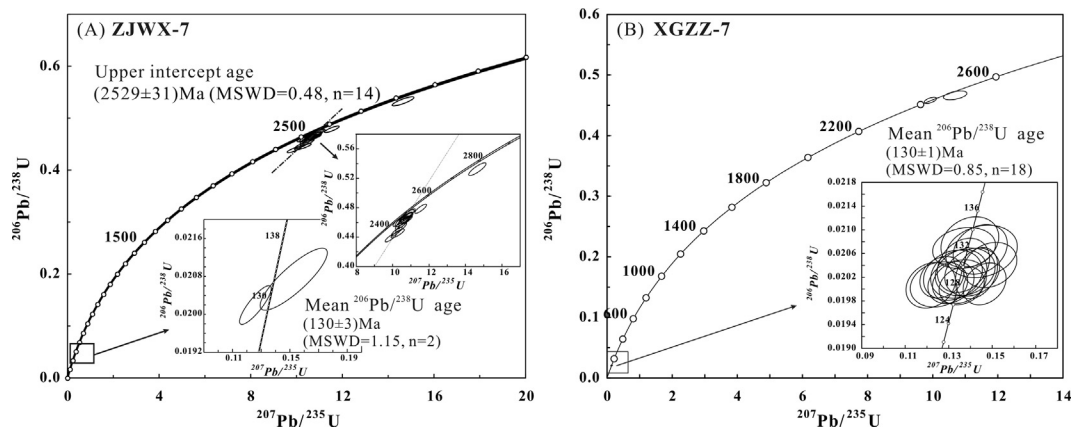

Fig. 8. LA-ICP-MS concordia diagrams showing zircon U-Pb ages for the Kuangshan pluton.

gram. Four spot analyses (spots 3 and 6–8) approximate the lower intercept with the Earth's lead evolution line because of their low common lead contents, whereas the remaining six spots with greater uncertainties deviate from the lower intercept. All spot analyses yield a lower intercept age of 131 ± 3.4 Ma (MSWD = 0.2), with the Y-intercept (initial ^{207}Pb/^{206}Pb) at 0.402 ± 0.018 (Fig. 6), representing their common-Pb components. Using the ^{207}Pb-correction method, the data yield a weighted mean ^{206}Pb/^{238}U age of 131 ± 3.9 Ma (MSWD = 0.1), which agrees well with the lower intercept age.

5.3. Zircon U-Pb ages

Zircon grains from the diorite sample (ZJWX-7) from the Zhangjiawa mine are colorless or light-brown, with lengths of 80–150 μm. They can be grouped into two categories on the basis of their morphologies and internal textures. Type 1 grains are short, subhedral prisms and mostly somewhat rounded with core-rim textures. Type 2 varieties are euhedral to subhedral, display patchy zoning and have bright rims in CL images (Fig. 7). Eighteen LA-ICP-MS spot analyses were made on 17 zircon grains including both types 1 and 2. They contain highly variable Th (14–690 ppm) and U (38–879 ppm), resulting in scattered Th/U ratios of 0.18–1.29 (Table. 3). Two spot analyses (spots 14 and 17 of type 2) plot on the concordia line and yield ^{206}Pb/^{238}U ages of 132 and 129 Ma, respectively. Fourteen spots, which have relatively low Th/U ratios, yield ^{207}Pb/^{206}Pb ages of 2469 to 2524 Ma. These old grains are distributed on a disconcordia with an upper intercept age of 2529 ± 31 Ma (MSWD = 0.48) (Fig. 8), and are

interpreted as ancient, inherited zircons. The remaining two zircons deviate slightly from the concordia and have ^{207}Pb/^{206}Pb ages of 2595 and 2816 Ma, and again are interpreted as inherited grains.

Zircon grains in sample (XZGZ-7) from the Xiaoguanzhuang mine are mostly subhedral to euhedral prisms, 100–200 μm long, with aspect ratios of about 3:1 to 1.5:1. In CL images, they are weakly zoned or show dark homogeneous absorption (Fig. 7). A few small, rounded crystals exhibit oscillatory zoning with dark rims and bright cores. A total of 20 spots were analyzed on 20 zircon grains. Eighteen grains have high Th (577–2260 ppm) and U (338–744 ppm) contents, with Th/U ratios of 1.7–3.42. Their ^{206}Pb/^{238}U ages range from 128 to 133 Ma and plot on the concordia line, with a weighted mean ^{206}Pb/^{238}U age of 130 ± 1 Ma (Fig. 8), which is interpreted as the emplacement age of the diorite. The remaining two grains (spots 2 and 19) have relatively low Th (88 and 262 ppm) and U (139 and 265 ppm), yielding lower Th/U ratios of 0.63 and 0.99. They yield ^{207}Pb/^{206}Pb ages of 2417 and 2513 Ma, and are interpreted as inherited grains.

6. Discussion

6.1. Hydrothermal origin of titanite

There are two possible origins for titanite crystals in the skarn assemblages: (1) relict grains or inclusions of magmatic grains transported by the mineralizing fluids that were subsequently entrained into the skarn assemblages, and (2) crystals precipitated directly from the hydrothermal fluids. Titanite grains from the
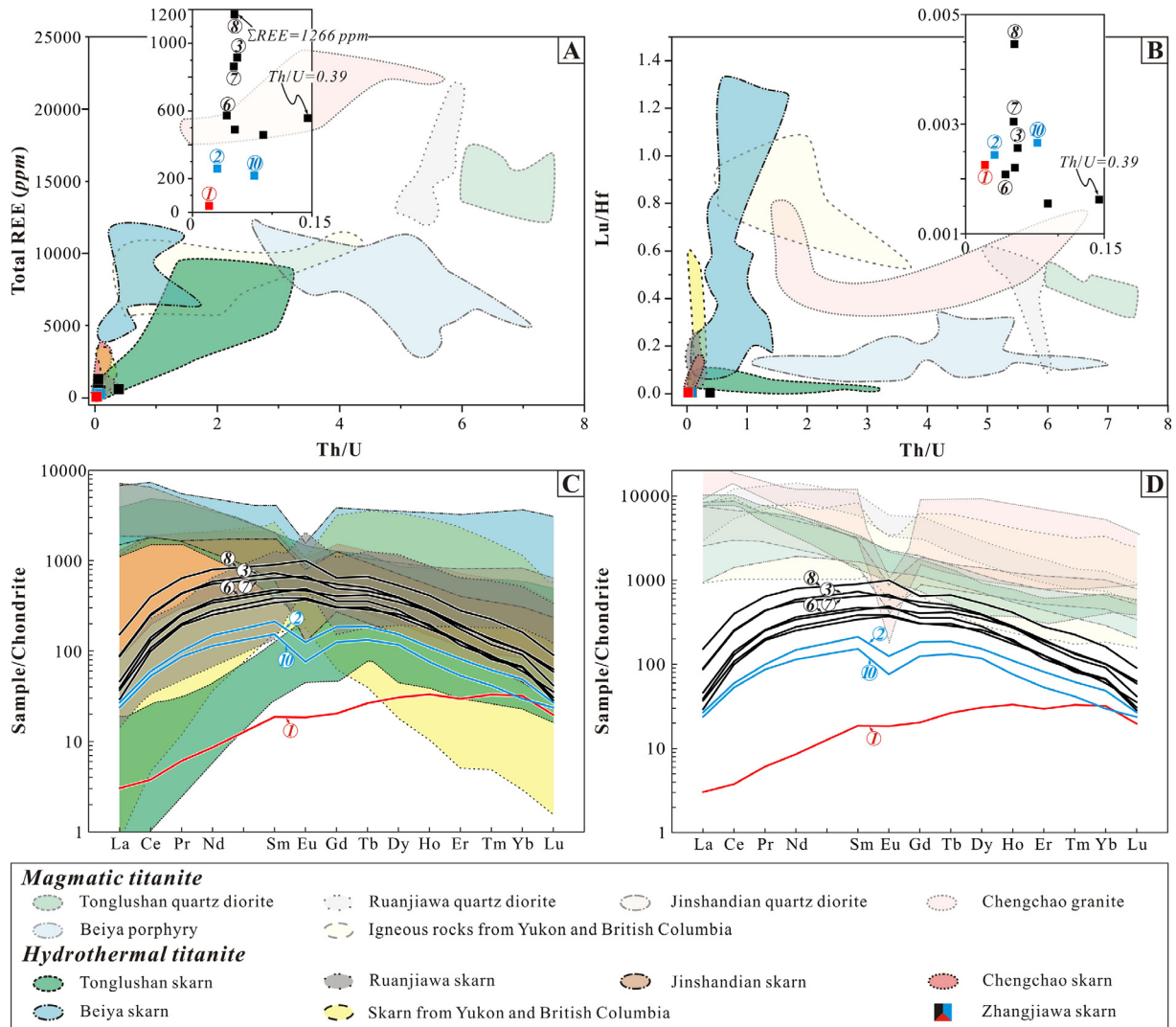
Fig. 9. Plots of Th/U versus total REE (A) and Lu/Hf (B), and chondrite-normalized REE patterns (C, D) showing distinct geochemical characteristics of magmatic and hydrothermal titanites. The values of other magmatic and hydrothermal titanites are from Li et al. (2010), Che et al. (2013), Zhu et al. (2014), Deng et al. (2015a), Fu et al. (2016), Hu et al. (2017). (Chondrite values are from Sun and McDonough (1989).)

Table 2
LA-ICPMS U-Pb isotope data for hydrothermal titanite from the Zhangjiawa deposit.

Sample No.	U	Th	Pb	Th/U	Measured isotopic ratios								^{207}Pb-Corrected ages (Ma)	
	ppm				^{207}Pb/^{206}Pb	1σ	^{207}Pb/^{235}U	1σ	^{206}Pb/^{238}U	1σ			^{206}Pb/^{238}U	1σ
0-22-36-Hydrothermal titanite														
0-22-36-*1*	18.57	0.39	2.92	0.02	0.1920	0.0272	0.8563	0.1062	0.0323	0.0023			122.6	18.1
0-22-36-*2*	72.52	2.28	10.42	0.03	0.1937	0.0238	0.9386	0.0932	0.0352	0.0027			132.2	18.1
0-22-36-*3*	156.42	8.84	9.66	0.06	0.0668	0.0065	0.1969	0.0181	0.0214	0.0008			129.4	5.5
0-22-36-*4*	87.81	4.69	12.37	0.05	0.1602	0.0183	0.6627	0.0662	0.0300	0.0017			131.1	12.4
0-22-36-*5*	36.23	3.23	5.75	0.09	0.1780	0.0198	0.8224	0.0777	0.0335	0.0021			135.5	14.6
0-22-36-*6*	119.17	5.16	9.90	0.04	0.0721	0.0080	0.2180	0.0228	0.0219	0.0009			130.6	6.3
0-22-36-*7*	168.51	8.78	13.45	0.05	0.0641	0.0034	0.1897	0.0094	0.0215	0.0005			131.0	3.1
0-22-36-*8*	259.09	13.71	20.85	0.05	0.0632	0.0042	0.1877	0.0116	0.0216	0.0006			131.9	3.9
0-22-36-*9*	11.55	4.46	1.99	0.39	0.1939	0.0328	0.9643	0.1471	0.0361	0.0027			135.5	23.5
0-22-36-*10*	50.95	3.97	9.46	0.08	0.2065	0.0190	1.0443	0.0790	0.0367	0.0021			129.5	14.4

endoskarn sample under investigation are subhedral to anhedral crystals with irregular zoning, and typically are intergrown with retrograde skarn minerals including chlorite, magnetite, phlogo-pite and minor epidote (Fig. 5). This textural relationship is consistent with a hydrothermal origin of these grains. It is noteworthy that some of the titanite grains contain baddeleyite (Fig. 5B),

Table 3
LA-ICPMS U-Pb isotope data for zircon from the diorite samples of Zhangjiawa and Xiaoguanzhuang mining areas.

Spot No.	Th	U	Th/U	$^{207}Pb/^{206}Pb$		$^{207}Pb/^{235}U$		$^{206}Pb/^{238}U$		$^{207}Pb/^{206}Pb$		$^{207}Pb/^{235}U$		$^{206}Pb/^{238}U$	
	ppm	ppm		Ratio	1σ	Ratio	1σ	Ratio	1σ	Age (Ma)	1σ	Age (Ma)	1σ	Age (Ma)	1σ
ZJWX-7-Zircon															
ZJWX-7-1	263	318	0.83	0.16593	0.00399	10.70211	0.25272	0.46276	0.00435	2517	40	2498	22	2452	19
ZJWX-7-2	202	373	0.54	0.16583	0.00352	10.90051	0.22734	0.47209	0.00423	2516	35	2515	19	2493	19
ZJWX-7-3	531	827	0.64	0.16519	0.00313	10.78573	0.20421	0.46878	0.00359	2510	33	2505	18	2478	16
ZJWX-7-4	261	290	0.90	0.16133	0.00333	10.34836	0.21964	0.46112	0.00422	2469	35	2466	20	2445	19
ZJWX-7-5	17	38	0.45	0.16639	0.00525	10.62820	0.32623	0.46396	0.00646	2522	48	2491	28	2457	28
ZJWX-7-6	88	220	0.40	0.16541	0.00392	10.78856	0.25768	0.47012	0.00472	2522	39	2505	22	2484	21
ZJWX-7-7	144	289	0.50	0.16624	0.00380	10.27707	0.24245	0.44501	0.00401	2520	39	2460	22	2373	18
ZJWX-7-8	322	337	0.96	0.16547	0.00340	10.69309	0.23698	0.46540	0.00501	2513	35	2497	21	2463	22
ZJWX-7-9	310	800	0.39	0.17386	0.00321	11.54018	0.21403	0.47859	0.00416	2595	31	2568	17	2521	18
ZJWX-7-10	14	76	0.18	0.16553	0.00379	10.55875	0.26440	0.45994	0.00605	2513	39	2485	23	2439	27
ZJWX-7-11	128	384	0.33	0.16648	0.00322	10.77960	0.21797	0.46632	0.00455	2524	27	2504	19	2467	20
ZJWX-7-12	173	878	0.20	0.16232	0.00337	9.89777	0.20491	0.43933	0.00388	2480	29	2425	19	2348	17
ZJWX-7-13	282	665	0.42	0.16517	0.00358	10.70703	0.23309	0.46684	0.00422	2510	37	2498	20	2470	19
ZJWX-7-14	439	394	1.12	0.05306	0.00523	0.15271	0.01548	0.02074	0.00043	332	219	144	14	132	3
ZJWX-7-15	690	879	0.78	0.16445	0.00303	10.22149	0.19398	0.44763	0.00409	2502	30	2455	18	2385	18
ZJWX-7-16	216	257	0.84	0.16657	0.00314	10.46923	0.19890	0.45323	0.00438	2524	31	2477	18	2410	19
ZJWX-7-17	619	482	1.29	0.04552	0.00270	0.12593	0.00729	0.02020	0.00027	–	–	120	7	129	2
ZJWX-7-18	35	105	0.33	0.19879	0.00431	14.65140	0.31474	0.53242	0.00573	2816	35	2793	20	2752	24
XGZZ-7-Zircon															
XGZZ-7-1	1354	540	2.51	0.04877	0.00289	0.13674	0.00794	0.02040	0.00030	200	133	130	7	130	2
XGZZ-7-2	88	139	0.63	0.16551	0.00377	10.68997	0.23870	0.46638	0.00481	2513	38	2497	21	2468	21
XGZZ-7-3	1747	619	2.82	0.05345	0.00298	0.14906	0.00810	0.02041	0.00025	346	131	141	7	130	2
XGZZ-7-4	577	338	1.70	0.05075	0.00376	0.14513	0.01085	0.02064	0.00029	228	168	138	10	132	2
XGZZ-7-5	1406	562	2.50	0.04939	0.00262	0.13596	0.00686	0.02006	0.00021	165	124	129	6	128	1
XGZZ-7-6	931	465	2.00	0.04785	0.00327	0.13706	0.00953	0.02069	0.00023	100	156	130	9	132	1
XGZZ-7-7	2224	744	2.99	0.04616	0.00251	0.12683	0.00668	0.02020	0.00023	6	126	121	6	129	1
XGZZ-7-8	1382	521	2.65	0.04742	0.00255	0.13105	0.00700	0.02011	0.00024	78	117	125	6	128	1
XGZZ-7-9	1406	518	2.72	0.05134	0.00302	0.14450	0.00821	0.02067	0.00028	257	132	137	7	132	2
XGZZ-7-10	1053	432	2.44	0.04583	0.00324	0.12552	0.00871	0.02008	0.00025	-	-	120	8	128	2
XGZZ-7-11	1110	433	2.56	0.04862	0.00314	0.13463	0.00855	0.02026	0.00027	128	148	128	8	129	2
XGZZ-7-12	976	489	2.00	0.04868	0.00295	0.13491	0.00816	0.02012	0.00025	132	202	128	7	128	2
XGZZ-7-13	1132	458	2.47	0.04940	0.00317	0.13971	0.00877	0.02079	0.00028	169	150	133	8	133	2
XGZZ-7-14	1077	471	2.29	0.04795	0.00328	0.13191	0.00893	0.02023	0.00028	98	152	126	8	129	2
XGZZ-7-15	1748	630	2.78	0.05064	0.00219	0.14276	0.00643	0.02027	0.00029	233	100	136	6	129	2
XGZZ-7-16	927	438	2.12	0.05073	0.00300	0.14080	0.00834	0.02029	0.00027	228	140	134	7	129	2
XGZZ-7-17	1285	535	2.40	0.04394	0.00268	0.12170	0.00750	0.02006	0.00025	-	-	117	7	128	2
XGZZ-7-18	2260	660	3.42	0.05357	0.00245	0.14651	0.00652	0.02009	0.00023	354	99	139	6	128	1
XGZZ-7-19	262	265	0.99	0.15637	0.00190	9.92779	0.12449	0.45820	0.00337	2417	21	2428	12	2432	15
XGZZ-7-20	899	438	2.05	0.05018	0.00344	0.13758	0.00908	0.02029	0.00027	211	159	131	8	129	2

which, however, is not observed in the ore-related dioritic intrusions. The contrasting occurrence suggests that the baddeleyite precipitated from zirconium-saturated, but silica-undersaturated, hydrothermal fluids. This in turn confirms a hydrothermal origin of the titanite grains.

Trace element compositions may provide additional evidence for the origin or formation environment of titanite (Li et al., 2010). Many studies have shown that hydrothermal titanite generally has lower Th contents and Th/U ratios (mostly < 1) compared to magmatic titanite (Fu et al., 2016). Titanite grains from the investigated endoskarn sample have extremely low Th/U (0.02–0.39) and Lu/Hf (0.0015–0.0045), generally comparable with hydrothermal titanite from skarn deposits elsewhere (Fig. 9A, B; Li et al., 2010; Che et al., 2013; Deng et al., 2015a; Fu et al., 2016; Hu et al., 2017). Similarly, hydrothermal titanite from the granite-related Big Bell gold deposit in Western Australia has low Th contents (generally < 10 ppm) and high U (103–1443 ppm), corresponding to very low Th/U ratios of 0.004–0.05 (Mueller and McNaughton, 2017). The low Th contents and low Th/U ratios in hydrothermal titanite most likely reflect the fact that Th is essentially an immobile element in hydrothermal fluids but U is mobile. This view is supported by many observations showing that hydrothermal zircons have much lower Th and Th/U ratios compared to their magmatic varieties, as is best illustrated by the Th/U ratios of the hydrothermal zircons (0.05–0.08) from oxidized

gold skarns of the Big Bell gold deposit coupled with much higher values of magmatic zircon crystals from the northwest granite (0.78), the lineated granodiorite (0.58) and the southeast granodiorite batholith (0.72) (cf. Mueller and McNaughton, 2017).

In addition, hydrothermal titanite grains from Zhangjiawa have low REE contents (36–1266 ppm), and are characterized by MREE enrichment excepting one grain (Fig. 9). This observation reflects preferential partition of MREE into titanite that precipitated from the fluid (Storey et al., 2007; Smith et al., 2009). The REE features of the hydrothermal titanite are distinctly different from those of magmatic titanite from many skarn related intrusions that typically show high REE contents and right-dipping REE patterns (e.g., Li et al., 2010; Deng et al., 2015a). The titanite grains from the investigated skarn have variable Eu anomalies (0.59–1.31; Fig. 9C, D), suggesting dynamic changes of oxygen fugacity of the ore-forming fluids during the mineralization. It has been shown that, under a reducing fluid, Eu is present mostly as Eu^{2+} that can be sufficiently incorporated into titanite precipitated from this fluid and thus positive Eu anomalies would be expected for the mineral (Horie et al., 2008). In contrast, titanite will show negative Eu anomalies if it precipitates from an oxidized fluid in which Eu is dominated by Eu^{3+} that cannot be accommodated in the mineral structure. Collectively, the textural and geochemical features support a hydrothermal origin for the studied titanite grains. It is noteworthy that one of the ten titanite grains (No. 1) has much lower

Th/U ratios, extremely low total REE contents and LREE (Fig. 9). The compositional difference likely reflects that this titanite grain precipitated from an evolving, REE-deficient fluid (Bau, 1991).

Titanite and baddeleyite of hydrothermal origin have also been found from iron skarns of the Daye district, Eastern China (Zhu et al., 2014; Hu et al., 2017), of the Nanling Range, South China (Zhao et al., 2016), and of the Handan-Xingtai district, North China (Deng et al., 2015b). In Zhangjiawa, hydrothermal Ti-oxides such as ilmenite, Mn-ilmenite, geikielite and rutile are intimately intergrown with magnetite (Fig. 4I-K). The widespread presence of the Ti-rich minerals and baddeleyite in Zhangjiawa demonstrates the mobility of Zr and Ti in the hydrothermal fluids that formed the iron skarn deposits. The mobility of Zr and Ti in skarn formation environments is thought to be a result of alkaline, halogen-rich (e.g., F, Cl) aqueous fluids (Gieré, 1990; Rubin et al., 1993; Van Baalen, 1993; Jiang et al., 2005; Migdisov et al., 2011; Deng et al., 2015b). A variety of F- and Cl-rich minerals (e.g., phlogopite, apatite, and scapolite; Fig. 4B-D, H) in the Zhangjiawa iron skarn deposit support such a fluid system.

6.2. Timing of iron skarn mineralization

Due to appreciable amounts of lattice-bound U and Th in titanite and the high closure temperature up to 700 °C for U-Pb isotopes in this mineral (Frost et al., 2001), titanite has recently been recognized as a robust U-Pb geochronometer for directly dating hydrothermal mineralization events (Storey et al., 2006; De Haller et al., 2006; Li et al., 2010; Deng et al., 2015a). In the present study, the paragenetic and textural characteristics demonstrate that hydrothermal titanite from the Zhangjiawa skarn formed during retrograde skarn alteration, broadly coeval with magnetite precipitation. Hence, the titanite U-Pb age (131.0 ± 3.9 Ma) can be reliably interpreted as the time of iron mineralization at Zhangjiawa. This view is confirmed by the consistency of the titanite U-Pb age of the iron skarn sample with the zircon U-Pb age of the ore-related Kuangshan intrusion (130 ± 1 Ma; Fig. 8).

6.3. Implications for the genesis of the ore-related magmas

Our new LA-ICP-MS zircon U-Pb data of the Kuangshan intrusion shows two age groups: (1) magmatic zircons with an age of

ca. 131 Ma, and (2) inherited Neoarchean and Paleoproterozoic zircons with ages mainly ranging from 2417 to 2595 Ma. Thus, emplacement of the Kuangshan pluton was coeval with the other Mesozoic plutons in the entire Laiwu ore field. For example, the early norite-diorite and late pyroxene-diorite of the Tietonggou intrusive complex (Fig. 2) have zircon U-Pb ages of 131.4 ± 4.9 Ma and 134.5 ± 2.3 Ma, respectively (Yang et al., 2006). Similarly, the Jiaoyu diorite pluton (Fig. 2) has a LA-ICP-MS zircon U-Pb age of 130 ± 2 Ma (Xu et al., 2004b). Therefore, the Mesozoic intrusive rocks in the Laiwu ore field were emplaced broadly contemporaneously between 130 and 135 Ma.

The age distribution of inherited zircons within intrusive rocks may provide useful information on the source of magmas (Keay et al., 1999). The group 2 zircons from the Kuangshan pluton are interpreted as xenocrysts from the NCC Archean basement with an age peak of ca. 2.5 Ga (Gao et al., 2004). The presence of Neoarchean zircons in the Kuangshan pluton is thought to reflect partial melting of the ancient lower crust. Such a mechanism of magma generation has recently been demonstrated for other early Cretaceous intrusive rocks of the same district. For example, Chen et al. (2013) found that the Tietonggou dioritic pluton is characterized by high Mg#s ([100 × molar Mg/(Mg + Fe)]), highly radiogenic Os isotopic compositions and negative correlations between Nd and Sr isotopic ratios. On the basis of these data, they suggested that the Tietonggou pluton most likely formed by mixing of siliceous crustal melts and basaltic magma derived from metasomatized mantle. This is also the case in the formation of the diorite in the western part of the Laiwu ore field, as partly indicated by the abundance of mafic microgranular enclaves in the host intrusion (Lan et al., 2013). Collectively, these observations suggest significant contributions of ancient lower crust of the NCC to the early Cretaceous magmatism associated with pervasive iron skarn mineralization in the Laiwu ore field.

6.4. A causal link between iron skarn mineralization and craton destruction

The iron skarn deposits in the NCC are mostly distributed within the western and eastern belts of the central-southern segment of the eastern NCC (Fig. 1). The western belt in the central part of the Trans-North China orogen comprises the South-
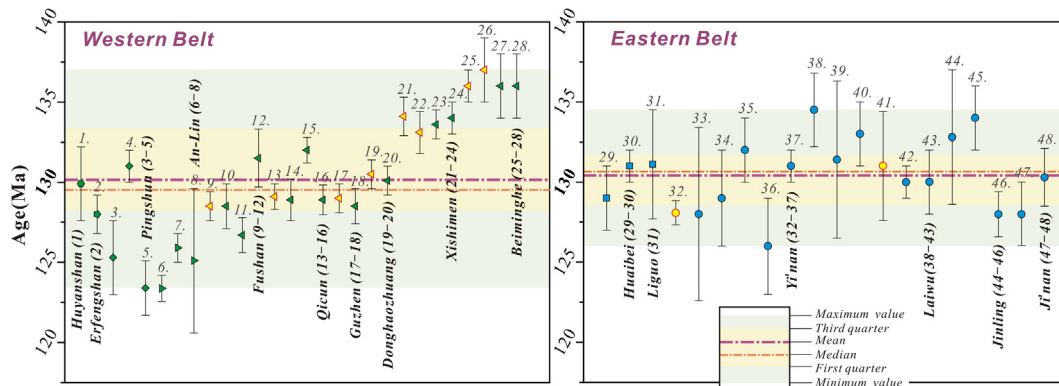

Fig. 10. Age distribution of iron skarn mineralization and ore-related magmatism in the western and eastern belts of the NCC. The yellow triangles (or circles) and other patterns represent the direct ore-forming ages and emplacement ages of the ore-related intrusions, respectively. For more details see Appendix (Table A.1). The isotope age data sources are as follows: Western belt: Taiyuan, Linfen (Huyanshan and Erfengshan, Ying et al., 2011), Pingshun (Wang et al., 2011a; Zhang et al., 2014a) and Handan-Xingtai ore fields (Chen et al., 2008a, 2014; Peng et al., 2004; Wang et al., 2006; Deng et al., 2014, 2015b; Sun et al., 2014; Zheng et al., 2007; Li et al., 2013a; Shen et al., 2013). Eastern belt: Xu-Huai (Yang et al., 2008; Xu et al., 2004a) and Luxi districts (Liu et al., 2014; Guo et al., 2014; Xu et al., 2004b; Yang et al., 2012; Yang et al., 2006; Jin et al., 2015; Guo et al., 2013; this study).

ern Taihang district, as well as the Linfen and Taiyuan ore fields. The Southern Taihang district, containing ∼1000 Mt high-grade iron ores (Yao et al., 1993), consists of the Handan-Xingtai, An-Lin, and Pingshun ore fields. $^{40}Ar/^{39}Ar$ dating of phlogopite associated with magnetite and U-Pb dating of hydrothermal zircon and allanite have shown that iron skarn mineralization in the Handan-Xingtai ore field occurred in a relatively small interval between 137 and 129 Ma (Zheng et al., 2007; Shen et al., 2013; Deng et al., 2014, 2015b), and was coeval with emplacement of intermediate-felsic intrusions in the same area (136–127 Ma; Peng et al., 2004; Chen et al., 2008a; Li et al., 2013a; Shen et al., 2013; Sun et al., 2014). No direct age constraints exist for iron skarn deposits of the An-Lin, Pingshun, Linfen, and Taiyuan ore fields, but a large collection of zircon U-Pb dates on the ore-related plutons (131–123 Ma; Peng et al., 2004; Wang et al., 2006; Wang et al., 2011a; Ying et al., 2011; Chen et al., 2014; Zhang et al., 2014a) suggests that they were broadly coeval with iron deposits in the Handan-Xingtai ore field.

Iron and Fe-polymetallic skarn deposits in the Luxi district of the eastern belt, with a total reserve of 760 Mt iron ores, are genetically associated with Mesozoic plutonic rocks ranging in composition from gabbro to diorite, granodiorite and monzonite. They cluster in the Jinan, Zibo and Laiwu ore fields. The Jinan and Jinling (Zibo) complexes, which are genetically related to the iron skarn deposits, have zircon U-Pb ages of 134–126 Ma (Yang et al., 2006; Guo et al., 2013; Yang et al., 2012; Jin et al., 2015), comparable with the ages of magmatism and iron mineralization in Laiwu (ca. 131 Ma; this study). To the southeast of the Luxi district, the Yi'nan Fe-Cu-Au skarn deposit has a molybdenite Re-Os age of 128.1 ± 0.8 Ma (Liu et al., 2014), and the ore-related Yi'nan intrusion has zircon U-Pb ages ranging from 132 to 126 Ma (Xu et al., 2004b; Yang et al., 2012; Guo et al., 2014). Farther south of the Luxi district, ore-related diorite intrusions associated with iron skarn deposits of the Xu-Huai district have zircon U-Pb ages of 131–129 Ma (Xu et al., 2004a; Yang et al., 2008). Taken together, the iron skarn deposits and associated intrusions in the eastern and western belts of North China craton took place coevally between ca. 135–125 Ma (Fig. 10). To the best of our knowledge, the early Cretaceous iron skarn deposits in NCC may represent the world's only large concentration of Phaneroic iron skarns hosted in Precambrian cratons.

Iron skarn mineralization throughout the NCC is temporally coincident with the widespread bimodal magmatism, rift basin development, and exhumation of metamorphic core complexes, combined marking the peak of lithospheric thinning and destruction of the NCC (Zhu et al., 2012b). We therefore suggest that the pervasive iron skarn mineralization was a product of lithospheric destruction of the NCC, which was ultimately triggered by westward subduction of the Izanagi plate beneath the eastern China continent (Zhu et al., 2015). Subduction and dehydration of the oceanic crust enriched and hydrated the ancient subcontinental lithospheric mantle beneath the NCC (Zhu et al., 2012a). Retreat of the subducting lithospheric plate (Zhu et al., 2015) was accompanied by upwelling of hot asthenosphere, leading to extensive partial melting of the fertile mantle lithosphere and formation of voluminous hydrous basaltic magmas. Underplating by the mafic magmas provided a heat source for partial melting of the lower continental crust to produce felsic melts, which subsequently mixed with the underplating mafic magmas to form hybrid magmas (Wu et al., 2005; Chen et al., 2007; Zhu et al., 2015). Iron-

rich magmatic-hydrothermal fluids exsolved during crystallization and cooling of the hybrid magmas, and interaction of such fluids with the evaporite-bearing, middle-lower Ordovician marine carbonate rocks have led to formation of the iron skarn deposits of the North China craton.

It is noteworthy that iron skarn and IOA (iron oxide-apatite) deposits are also widely distributed in the Daye (Li et al., 2014), Ningwu (Zhou et al., 2011, 2013), and Luzong districts (Zhou et al., 2010, 2011) along the Middle-Lower Yangtze Metallogenic Belt, immediately to the southeast of the North China craton (Fig. 1). These deposits also formed at ca. 130 Ma (Zhou et al., 2011, 2013; Li et al., 2014; Zhu et al., 2017), coincident with iron skarn mineralization in North China craton. This temporal and spatial coincidence further confirm that the subduction of the paleo-Pacific plate has been the fundamental control in the formation of the giant iron belt in Eastern China.

7. Conclusions

Textural and geochemical data suggest that titanite grains contained in mineralized skarn of the Zhangjiawa iron deposit, Luxi district, eastern North China craton are of hydrothermal origin and have precipitated directly from ore-forming fluids. The hydrothermal titanite has a concordant U-Pb age of 131.0 ± 3.9 Ma (n = 10, MSWD = 0.1, 1σ), which is consistent with the zircon U-Pb age (130 ± 1 Ma) of the ore-related Kuangshan pluton. The age data thus confirm a temporal and likely genetic link between the iron skarn mineralization and spatially associated intrusions in the Laiwu ore field. The presence of abundant Neoarchean inherited zircons in ore-related intrusions, as revealed in this study and widely recognized in previous investigations of the other intrusions, confirms a whole-scale contribution of ancient lower crust of the NCC in the Mesozoic magmatism and associated iron skarn mineralization. Synthesis of existing radiometric age data suggests that iron skarn mineralization and associated magmatism in the eastern and western belts of the NCC took place coevally between 135 and 125 Ma, with a peak at ca. 130 Ma. This pervasive iron skarn mineralization and associated magmatic events coincide in time with the peak of lithospheric thinning and destruction of the NCC, thus demonstrating a likely causal link between the two.

Acknowledgements

Appendix A

Table A.1

Table A.1

Age data of the Mesozoic iron skarn deposits and related intrusions in the NCC.

Belt	District	Ore field	Intrusion/Deposit	No.	Sample	Analytical methods	Age (Ma)	Reference
Western Belt		Tiyuan	Huyanshan	1	Monzonite	A	129.9 ± 2.3	Ying et al. (2011)
		Linfen	Erfengshan	2	Quartz monzonite	A	128 ± 1.2	
	Southern Taihang	Pingshun	Xi'anli	3	Diorite	A	125.5 ± 2.3	Zhang et al. (2014)
				4	Hornblende gabbro	A	131 ± 1	Wang et al. (2011a)
				5	Olivine gabbro	A	123.4 ± 1.7	Zhang et al. (2014a)
		An-Lin	Lizhen	6	Porphyritic diorite	A	123.38 ± 0.81	Chen et al. (2014)
			Dongye	7	Hornblende diorite	A	125.9 ± 0.9	Peng et al. (2004)
				8	Gabbro	A	125.2 ± 4.5	Wang et al. (2006)
		Handan-Xingtai	Fushan	9	Skarn	C	128.5 ± 0.9	Deng et al. (2015b)
				10	Diorite	A	128.5 ± 1.4	
				11	Hornblende diorite	A	126.7 ± 1.1	Peng et al. (2004)
				12	Gabbroic diorite	A	131.5 ± 1.8	Chen et al. (2008a,b)
			Qicun	13	Skarn	C	129.1 ± 0.8	Deng et al. (2015b)
				14	Monzodiorite	A	128.9 ± 1.3	
				15	Monzonite	A	132 ± 0.8	Chen et al. (2008a,b)
				16	Biotite diorite	A	128.9 ± 0.93	Sun et al. (2014)
			Guzhen	17	Skarn	C	129 ± 0.9	Deng et al. (2015b)
				18	Monzonite	A	128.5 ± 1.1	
			Donghao zhuang	19	Skarn	C	130.5 ± 0.9	
				20	Diorite	A	130.1 ± 0.9	
			Xishimen	21	Skarn	C	134.1 ± 1.2	
				22	Skarn	F	133.1 ± 1.3	Zheng et al. (2007)
				23	Monzonite	A	133.6 ± 0.9	Deng et al. (2015)
				24	Altered porphyritic diorite	A	134 ± 1	Li et al. (2013a)
			Beiminghe	25	Skarn	D	136 ± 1	Deng et al. (2014)
				26	Skarn	F	137 ± 2	Shen et al. (2013)
				27	Altered porphyritic diorite	A	136 ± 2	
				28	Diorite	A	136 ± 2	Deng et al. (2014)
Eastern Belt	Xu-Huai	Huaibei	Fengshan	29	Porphyritic monzodiorite	A	129 ± 2	Yang et al. (2008)
			Caishan	30	Porphyritic quartz diorite	A	131 ± 1	
		Xuzhou	Liguo	31	Porphyritic diorite	A	131.1 ± 3.4	Xu et al. (2004a)
	Luxi	Yi'nan	Jinchang	32	Ores	G	128.1 ± 0.8	Liu et al. (2014)
			Jinlong	33	Porphyritic diorite	A	128 ± 5.4	Guo et al. (2014)
			Tongjing	34	Diorite	A	129 ± 3	Xu et al. (2004b)
			Yinshan zhuang	35	Medium-grained diorite	A	132 ± 2	
			Chaoyang	36	Coarse-grained diorite	A	126 ± 3	
			Shangyu	37	Gabbro	A	131 ± 1	Yang et al. (2012)
		Laiwu	Tietonggou	38	Pyroxene-diorite	A	134.5 ± 2.3	Yang et al. (2006)
				39	Norite-diorite	A	131.4 ± 4.9	
				40	Gabbroic diorite	A	133 ± 2	Yang et al. (2012)
			Zhangjiawa	41	Skarn	E	131 ± 3.4	Thsi study
			Kuangshan	42	Diorite	A	130 ± 1	
			Jiaoyu	43	Porphyritic diorite	A	130 ± 2	Xu et al. (2004b)
		Zibo	Jinling	44	Biotite diorite	A	132.8 ± 4.2	Yang et al. (2006)
				45	Gabbroic diorite	A	134 ± 2	Yang et al. (2012)
		Jinan		46	Biotite diorite	A	126 ± 1.5	Jin et al. (2015)
				47	Monzonite	A	128 ± 1.4	
				48	Gabbro	B	130.3 ± 1.8	Guo et al. (2013)

Analytical methods: Magmatic zircon (A) and baddeleyite (B) U-Pb dating; U-Pb dating of hydrothermal U-bearing accessory minerals (C-zircon; D-allanite-(La); E-titanite); F-Phlogopite ^{40}Ar-^{39}Ar dating; G-Molybdenite Re-Os dating.

References

Andersen, T., 2002. Correction of common lead in U-Pb analyses that do not report ^{204}Pb. Chem. Geol. 192 (1), 59–79.

Bau, M., 1991. Rare-earth element mobility during hydrothermal and metamorphic fluid-rock interaction and the significance of the oxidation state of europium. Chem. Geol. 93 (3–4), 219–230.

Charles, N., Gumiaux, C., Augier, R., Chen, Y., Faure, M., Lin, W., Zhu, R.X., 2012. Metamorphic core complex dynamic and structural development: field evidence from the Liaodong Peninsula (China, East Asian). Tectonophys 560, 22–50.

Che, X.D., Linnen, R.L., Wang, R.C., Groat, L.A., Brand, A.A., 2013. Distribution of trace and rare earth elements in titanite from tungsten and molybdenum deposits in Yukon and British Columbia, Canada. Can. Mineral. 51 (3), 415–438.

Chen, B., Zhai, M.G., Tian, W., 2007. Origin of the Mesozoic magmatism in the North China Craton: constraints from petrological and geochemical data. Geol. Soc., London, Spec. Publ. 280 (1), 131–151.

Chen, B., Tian, W., Jahn, B.M., Chen, Z.C., 2008a. Zircon SHRIMP U-Pb ages and in-situ Hf isotopic analysis for the Mesozoic intrusions in South Taihang, North China craton: evidence for hybridization between mantle-derived magmas and crustal components. Lithos 102 (1), 118–137.

Chen, L., Tao, W., Zhao, L., Zhen, T.Y., 2008b. Distinct lateral variation of lithospheric thickness in the Northeastern North China Craton. Earth Planet. Sci. Lett. 267, 56–68.

Chen, B., Jahn, B.M., Suzuki, K., 2013. Petrological and Nd-Sr-Os isotopic constraints on the origin of high-Mg adakitic rocks from the North China Craton: tectonic implications. Geology 41 (1), 91–94.

Chen, Y., Zhang, Z.C., Zhu, J., 2014. Geochronology of the Anlin iron skarn deposit, Henan Province and insight into the sources of iron. Acta Petrol. Sin. 30 (5), 1307–1321.

De Haller, A., Corfu, F., Fontboté, L., Schaltegger, U., Barra, F., Chiaradia, M., Frank, M., Alvarado, J.Z., 2006. Geology, geochronology, and Hf and Pb isotope data of the Raúl-Condestable iron oxide-copper-gold deposit, central coast of Peru. Econ. Geol. 101 (2), 281–310.

Deng, X.D., Li, J.W., Wen, G., 2014. Dating iron skarn mineralization using hydrothermal allanite-(La) U-Th-Pb isotopes by laser ablation ICP-MS. Chem. Geol. 382, 95–110.

Deng, X.D., Li, J.W., Zhou, M.F., Zhao, X.F., Yan, D.R., 2015a. In-situ LA-ICPMS trace elements and U-Pb analysis of titanite from the Mesozoic Ruanjiawan W-Cu-Mo skarn deposit, Daye district, China. Ore Geol. Rev. 65, 990–1004.

Deng, X.D., Li, J.W., Wen, G., 2015b. U-Pb Geochronology of Hydrothermal Zircons from the Early Cretaceous Iron Skarn Deposits in the Handan-Xingtai District, North China Craton. Econ. Geol. 110 (8), 2159–2180.

Fei, X.H., Zhang, Z.C., Han, L., 2014. Mineralogy of the Zhangjiawa skarn iron deposit in Shandong Province and its implications for metallogenic environment. Geol. China 41 (6), 1873–1896 (in Chinese with English abstract).

Frost, B.R., Chamberlain, K.R., Schumacher, J.C., 2001. Sphene (titanite): phase relations and role as a geochronometer. Chem. Geol. 172 (1), 131–148.

Fu, Y., Sun, X.M., Zhou, H.Y., Lin, H., Yang, T.J., 2016. In-situ LA-ICP-MS U-Pb geochronology and trace elements analysis of polygenetic titanite from the giant Beiya gold-polymetallic deposit in Yunnan Province, Southwest China. Ore Geol. Rev. 77, 43–56.

Gao, S., Rudnick, R.L., Yuan, H.L., Liu, X.M., Liu, Y.S., Xu, W.L., Ling, W.L., Ayers, J., Wang, X.C., Wang, Q.H., 2004. Recycling lower continental crust in the North China craton. Nature 432 (7019), 892–897.

Gieré, R., 1990. Hydrothermal mobility of Ti, Zr and REE: examples from the Bergell and Adamello contact aureoles (Italy). Terra Nova 2 (1), 60–67.

Griffin, W.L., Andi, Z., O'Reilly, S.Y., Ryan, C.G., 1998. Phanerozoic evolution of the lithosphere beneath the Sino-Korean craton. In: Mantle dynamics and plate interactions in East Asia, pp. 107–126.

Griffin, W.L., Powell, W.J., Pearson, N.J., O'Reilly, S.Y., 2008. GLITTER: data reduction software for laser ablation ICP-MS. Laser Ablation-ICP-MS in the earth sciences. Mineralogical association of Canada short course series, 40, pp. 204–207.

Groves, D.I., Bierlein, F.P., 2007. Geodynamic settings of mineral deposit systems. J. Geol. Soc. 164 (1), 19–30.

Guo, F., Guo, J.T., Wang, C.Y., Fan, W.M., Li, C.M., Zhao, L., Li, H.X., Li, J.Y., 2013. Formation of mafic magmas through lower crustal AFC processes-An example from the Jinan gabbroic intrusion in the North China Block. Lithos 179, 157–174.

Guo, P., Santosh, M., Li, S.R., Li, Q., 2014. Crustal evolution in the central part of Eastern NCC: Zircon U-Pb ages from multiple magmatic pulses in the Luxi area and implications for gold mineralization. Ore Geol. Rev. 60, 126–145.

Horie, K., Hidaka, H., Gauthier-Lafaye, F., 2008. Elemental distribution in apatite, titanite and zircon during hydrothermal alteration: durability of immobilization mineral phases for actinides. Phys. Chem. Earth. 33, 962–968.

Hu, Z.C., Gao, S., Liu, Y.S., Hu, S.H., Chen, H.H., Yuan, H.L., 2008. Signal enhancement in laser ablation ICP-MS by addition of nitrogen in the central channel gas. J. Anal. Atom. Spectrom. 23 (8), 1093–1101.

Hu, H., Li, J.W., McFarlane, C.R.M., 2017. Hydrothermal titanite from the Chengchao iron skarn deposit: temporal constraints on iron mineralization, and its potential as a reference material for titanite U-Pb dating. Miner. Petrol. http:// dx.doi.org/10.1007/s00710-017-0517-z.

Jiang, S.Y., Wang, R.C., Xu, X.S., Zhao, K.D., 2005. Mobility of high field strength elements (HFSE) in magmatic-, metamorphic-, and submarine-hydrothermal systems. Phys. Chem. Earth, Parts A/B/C 30 (17), 1020–1029.

Jin, Z.L., Zhang, Z.C., Hou, T., Santosh, M., Han, L., 2015. Genetic relationship of high-Mg dioritic pluton to iron mineralization: a case study from the Jinling skarn-type iron deposit in the North China Craton. J. Asian Earth Sci. 113, 957–979.

Keay, S., Steele, D., Compston, W., 1999. Identifying granite sources by SHRIMP U-Pb zircon geochronology: an application to the Lachlan foldbelt. Contrib. Mineral. Petrol. 137 (4), 323–341.

Lan, T.G., Fan, H.R., Santosh, M., Hu, F.F., Yang, K.F., Yang, Y.H., Liu, Y.S., 2013. Crust-mantle interaction beneath the Luxi Block, eastern North China Craton: evidence from coexisting mantle- and crust-derived enclaves in a quartz monzonite pluton. Lithos 177, 1–16.

Li, S.R., Santosh, M., 2014. Metallogeny and craton destruction: records from the North China Craton. Ore Geol. Rev. 56, 376–414.

Li, J.W., Deng, X.D., Zhou, M.F., Liu, Y.S., Zhao, X.F., Guo, J.L., 2010. Laser ablation ICP-MS titanite U-Th-Pb dating of hydrothermal ore deposits: a case study of the Tonglushan Cu-Fe-Au skarn deposit, SE Hubei Province, China. Chem. Geol. 270 (1), 56–67.

Li, J.W., Bi, S.J., Selby, D., Chen, L., Vasconcelos, P., Thiede, D., Zhou, M.F., Zhao, X.F., Li, Z.K., Qiu, H.N., 2012. Giant Mesozoic gold provinces related to the destruction of the North China craton. Earth Planet. Sci. Lett. 349–350, 26–37.

Li, S.R., Santosh, M., Zhang, H.F., Shen, J.F., Dong, G.C., Wang, J.Z., Zhang, J.Q., 2013a. Inhomogeneous lithospheric thinning in the central North China Craton: zircon U-Pb and S-He-Ar isotopic record from magmatism and metallogeny in the Taihang Mountains. Gondwana Res. 23 (1), 141–160.

Li, Z.K., Li, J.W., Zhao, X.F., Zhou, M.F., Selby, D., Bi, S.J., Sui, J.X., Zhao, Z.J., 2013b. Crustal-Extension Ag-Pb-Zn Veins in the Xiong'ershan District, Southern North China Craton: constraints from the Shagou Deposit. Econ. Geol. 108 (7), 1703–1729.

Li, J.W., Vasconcelos, P.M., Zhou, M.F., Deng, X.D., Cohen, B., Bi, S.J., Zhao, X.F., Selby, D., 2014. Longevity of magmatic-hydrothermal systems in the Daye Cu-Fe-Au District, eastern China with implications for mineral exploration. Ore Geol. Rev. 57, 375–392.

Liu, J.L., Davis, G.A., Lin, Z.Y., Wu, F.Y., 2005. The Liaonan metamorphic core complex, southeastern Liaoning Province, North China: a likely contributor to Cretaceous rotation of eastern Liaoning, Korea and contiguous areas. Tectonophysics 407, 65–80.

Liu, Y.S., Hu, Z.C., Gao, S., Gunther, D., Xu, J., Gao, C.G., Chen, H.H., 2008. In situ analysis of major and trace elements of anhydrous minerals by LA-ICP-MS without applying an internal standard. Chem. Geol. 257 (1–2), 34–43.

Liu, Y.S., Gao, S., Hu, Z.C., Gao, C.G., Zong, K.Q., Wang, D.B., 2010. Continental and oceanic crust recycling-induced melt-peridotite interactions in the Trans-North China Orogen: U-Pb dating, Hf isotopes and trace elements in zircons from mantle xenoliths. J. Petrol. 51 (1–2), 537–571.

Liu, Y., Santosh, M., Li, S.R., Guo, P., 2014. Stable isotope geochemistry and Re-Os ages of the Yinan gold deposit, Shandong Province, northeastern China. Int. Geol. Rev. 56 (6), 695–710.

LMM Corp., (Luzhong Metallurgy & Mining Corporation) 2009. Resources reserve annual report (2008) of Zhangjiawa I, II, III mining districts in Laiwu city, Shandong province. Unpublished report, Shandong, pp 14–24 (in Chinese).

Ludwig, K.R., 2003. Isoplot 3.0: a geochronological toolkit for Microsoft Excel. Berkeley Geochronology Center Special Publications 4.

Meng, Q.L., 1988. On polygene of Laiwu magmatic complex in Shandong Province. J. Changchun Univ. Earth Sci. 18 (1), 43–52 (in Chinese with English abstract).

Menzies, M.A., Xu, Y.G., 1998. Geodynamics of the North China craton. In: Mantle dynamics and plate interactions in East Asia, pp. 155–165.

Migdisov, A.A., Williams-Jones, A.E., Van Hinsberg, V., Salvi, S., 2011. An experimental study of the solubility of baddeleyite (ZrO2) in fluoride-bearing solutions at elevated temperature. Geochim. Cosmochim. Acta 75 (23), 7426–7434.

Mueller, A.G., McNaughton, N.J., 2017. Mineral equilibria and zircon, garnet and titanite U-Pb ages constraining the PTt path of granite-related hydrothermal systems at the Big Bell gold deposit, Western Australia. Miner. Deposita. http:// dx.doi.org/10.1007/s00126-017-0722-z.

Peng, T.P., Wang, Y.J., Fan, W.M., Guo, F., Peng, B.X., 2004. SHRIMP zircon U-Pb geochronology of the diorites for southern Taihang Mountains in the North China Interior and its petrogenesis. Acta Petrol. Sin. 20 (5), 1253–1262 (in Chinese with English abstract).

Rubin, J.N., Henry, C.D., Price, J.G., 1993. The mobility of zirconium and other "immobile" elements during hydrothermal alteration. Chem. Geol. 110 (1), 29–47.

Shen, J.F., Santosh, M., Li, S.R., Zhang, H.F., Yin, N., Dong, G.C., Wang, Y.J., Ma, G.G., Yu, H.J., 2013. The Beiminghe skarn iron deposit, eastern China: geochronology, isotope geochemistry and implications for the destruction of the North China Craton. Lithos 156, 218–229.

Smith, M.P., Storey, C.D., Jeffries, T.E., Ryan, C., 2009. In Situ U-Pb and Trace Element Analysis of Accessory Minerals in the Kiruna District, Norrbotten, Sweden: new Constraints on the Timing and Origin of Mineralization. J. Petrol. 50 (11), 2063–2094.

Stacey, J.T., Kramers, J.D., 1975. Approximation of terrestrial lead isotope evolution by a two-stage model. Earth Planet. Sci. Lett. 26 (2), 207–221.

Storey, C.D., Jeffries, T.E., Smith, M., 2006. Common lead-corrected laser ablation ICP-MS U-Pb systematics and geochronology of titanite. Chem. Geol. 227 (1), 37–52.

Storey, C.D., Smith, M.P., Jeffries, T.E., 2007. In situ LA-ICP-MS U-Pb dating of metavolcanics of Norrbotten, Sweden: records of extended geological histories in complex titanite grains. Chem. Geol. 240 (1–2), 163–181.

Sun, S.S., McDonough, W.F., 1989. Chemical and isotopic systematics of oceanic basalts: implications for mantle composition and processes. Geol. Soc., London, Spec. Publ. 42 (1), 313–345.

Sun, J.F., Yang, J.H., Wu, F.Y., Li, X.H., Yang, Y.H., Xie, L.W., Wilde, S.A., 2010. Magma mixing controlling the origin of the Early Cretaceous Fangshan granitic pluton, North China Craton: in situ U-Pb age and Sr-, Nd-, Hf- and O-isotope evidence. Lithos 120 (3–4), 421–438.

Sun, Y., Xiao, L., Zhu, D., Wu, T., Deng, X.D., Bai, M., Wen, G., 2014. Geochemical, geochronological, and Sr-Nd-Hf isotopic constraints on the petrogenesis of the Qicun intrusive complex from the Handan-Xingtai district: implications for the mechanism of lithospheric thinning of the North China Craton. Ore Geol. Rev. 57, 363–374.

Tang, L.C., 1996. The Paleozoic ore-bearing sedimentary formations of nonmetallic minerals in western Shandong. J. Shandong Geol. 12 (2), 48–61 (in Chinese with English abstract).

Tera, F., Wasserburg, G.J., 1972. U-Th-Pb systematics in three Apollo 14 basalts and the problem of initial Pb in lunar rocks. Earth Planet. Sci. Lett. 14 (3), 281–304.

Van Baalen, M.R., 1993. Titanium mobility in metamorphic systems: a review. Chem. Geol. 110 (1–3), 233–249.

Wang, Y.J., Fan, W.M., Zhang, H.F., Peng, T.P., 2006. Early Cretaceous gabbroic rocks from the Taihang Mountains: implications for a paleosubduction-related lithospheric mantle beneath the central North China Craton. Lithos 86 (3), 281–302.

Wang, C.G., Xu, W.L., Wang, F., Yang, D.B., 2011a. Petrogenesis of the early Cretaceous Xi'anli hornblende-gabbros from the southern Taihang Mountains: evidence from zircon U-Pb geochronology, Hf isotope and whole-rock geochemistry. Earth Sci.-J. China Univ. Geosci. 36 (3), 471–482 (in Chinese with English abstract).

Wang, T., Zheng, Y.D., Zhang, J.J., Zeng, L.S., Donskaya, T., Guo, L., Li, J.B., 2011b. Pattern and kinematic polarity of late Mesozoic extension in continental NE Asia: perspectives from metamorphic core complexes. Tectonics 30 (6).

Wiedenbeck, M., Allé, P., Corfu, F., Griffin, W.L., Meier, M., Oberli, F., Quadt, A.V., Roddick, J.C., Spiegel, W., 1995. Three natural zircon standards for U-Th-Pb, Lu-Hf, trace element and REE analyses. Geostand. Geoanal. Res. 19 (1), 1–23.

Williams, I.S., 1998. U-Th–Pb geochronology by ion microprobe. In: McKibben, M.A., Shanks III, W.C., Ridley, W.I. (Eds.), Applications of Microanalytical Techniques to Understanding Mineralizing Processes: Reviews in Economic Geology, 7, pp. 1–35.

Wu, F.Y., Lin, J.Q., Wilde, S.A., Zhang, X.O., Yang, J.H., 2005. Nature and significance of the Early Cretaceous giant igneous event in eastern China. Earth Planet. Sci. Lett. 233 (1), 103–119.

Xu, W.L., Wang, Q.H., Liu, X.C., Wang, D.Y., Guo, J.H., 2004a. Chronology and sources of Mesozoic intrusive complex in Xu-Huai region, central China: constraints from SHRIMP zircon U-Pb dating. Acta Geol. Sinica 78 (1), 96–106.

Xu, Y.G., Huang, X.L., Ma, J.L., Wang, Y.B., Iizuka, Y., Xu, J.F., Wang, Q., Wu, X.Y., 2004b. Crust-mantle interaction during the tectono-thermal reactivation of the North China Craton: constraints from SHRIMP zircon U-Pb chronology and geochemistry of Mesozoic plutons from western Shandong. Contrib. Mineral. Petr. 147 (6), 750–767.

Yang, Z.Y., Cheng, Y.Q., Wang, H.Z., 1986. The Geology of China. Oxford University Press, New York, p. 306.

Yang, J.H., Wu, F.Y., Wilde, S.A., 2003. A review of the geodynamic setting of large-scale Late Mesozoic gold mineralization in the North China Craton: an association with lithospheric thinning. Ore Geol. Rev. 23 (3), 125–152.

Yang, C.H., Xu, W.L., Yang, D.B., Liu, C.C., Liu, X.M., Hu, Z.C., 2006. Petrogenesis of the mesozoic high-Mg diorites in west Shandong: evidence from chronology and petro-geochemistry. Earth Sci.-J. China Univ. Geosci. 31 (1), 81–92 (in Chinese with English abstract).

Yang, D.B., Xu, W.L., Pei, F.P., Wang, Q.H., Gao, S., 2008. Chronology and Pb isotope compositions of Early Cretaceous adakitic rocks in Xuzhou-Huaibei area, central China: constraints on magma sources and tectonic evolution in the eastern North China Craton. Acta Petrol. Sin. 24 (8), 1745–1758 (in Chinese with English abstract).

Yang, Y.H., Wu, F.Y., Wilde, S.A., Liu, X.M., Zhang, Y.B., Xie, L.W., Yang, J.H., 2009. In situ isotopic constraints on the petrogenesis of the Ordovician Mengyin kimberlites in the North China Craton. Chem. Geol. 264 (1–4), 24–42.

Yang, Q.L., Zhao, Z.F., Zheng, Y.F., 2012. Slab–mantle interaction in continental subduction channel: geochemical evidence from Mesozoic gabbroic intrusives in southeastern North China. Lithos 155, 442–460.

Yao, P.H., Wang, K.N., Du, C.L., Lin, Z.T., Song, X., 1993. Records of China's Iron Ore Deposits. Metallurgical Industry Press (in Chinese), Beijing.

Ying, J.F., Zhang, H.F., Tang, Y.F., 2011. Crust-mantle interaction in the central North China Craton during the Mesozoic: evidence from zircon U-Pb chronology, Hf isotope and geochemistry of syenitic-monzonitic intrusions from Shanxi province. Lithos 125 (1), 449–462.

Zeng, G.X., Lu, C., Xu, J.F., 1998. Geology of iron deposits in Shandong. Shandong Science and Technology Press, Jinan, pp. 4–84 (in Chinese with English abstract).

Zhang, H.D., Liu, J.C., Chen, Z.L., Chen, B.L., Peng, S.X., Men, W.H., 2014a. Petrogenesis of the Pingshun complexes in the southern Taihan Mountains: petrology, geochronology and geochemistry. Geotect. et Metallog. 38 (2), 454–471 (in Chinese with English abstract).

Zhang, Z.C., Hou, T., Santosh, M., Li, H.M., Li, J.W., Zhang, Z.H., Song, X.Y., Wang, M., 2014b. Spatio-temporal distribution and tectonic settings of the major iron deposits in China: an overview. Ore Geol. Rev. 57, 247–263.

Zhao, G.C., Wilde, S.A., Cawood, P.A., Sun, M., 2001. Archean blocks and their boundaries in the North China Craton: lithological, geochemical, structural and P-T path constraints and tectonic evolution. Precambrian Res. 107 (1–2), 45–73.

Zhao, G.C., Sun, M., Wilde, S.A., Li, S.Z., 2005. Late Archean to Paleoproterozoic evolution of the North China Craton: key issues revisited. Precambrian Res. 136 (2), 177–202.

Zhao, W.W., Zhou, M.F., Chen, W.T., 2016. Growth of hydrothermal baddeleyite and zircon in different stages of skarnization. Am. Mineral. 101 (12), 2689–2700.

Zheng, J.M., Xie, G.Q., Liu, J., Chen, M.H., Wang, S.M., Guo, S.F., Gao, X., Li, G.D., 2007. ^{40}Ar-^{39}Ar dating of phlogopite from the Xishimen skarn deposit in the Handan-Xingtai area, southern Hebei, and its implications. Acta Petrol. Sin. 23 (10), 2513–2518 (in Chinese with English abstract).

Zhou, T.F., Fan, Y., Yuan, F., Song, C.Z., Zhang, L.J., Qian, C.C., Lu, S.M., Cooke, D.R., 2010. Temporal-spatial framework of magmatic intrusions in Luzong volcanic basin in East China and their constrain to mineralizations. Acta Petrol. Sin. 26 (9), 2694–2714 (in Chinese with English abstract).

Zhou, T.F., Fan, Y., Yuan, F., Zhang, L.J., Ma, L., Qian, B., Xie, J., 2011. Petrogensis and metallogeny study of the volcanic basins in the Middle and Lower Yangtze metallogenic belt. Acta Geol. Sin. 85 (5), 712–730 (in Chinese with English abstract).

Zhou, T.F., Fan, Y., Yuan, F., Zhang, L.J., Qian, B., Ma, L., Yang, X.F., 2013. Geology and geochronology of magnetite-apatite deposits in the Ning-Wu volcanic basin, eastern China. J. Asian Earth Sci. 2013 (66), 90–107.

Zhu, G., Song, C.Z., Niu, M.L., Liu, G.S., Wang, Y.S., 2002. Lithospheric textures of the Tan-Lu Fault Zone and their genetic analysis. Geol. J. China Univ. 8, 248–256 (in Chinese with English abstract).

Zhu, G., Liu, G.S., Niu, M.L., Song, C.Z., Wang, D.X., 2003. Transcurrent movement and genesis of the Tan-Lu fault zone. Geol. Bull. China 22, 200–207 (in Chinese with English abstract).

Zhu, R.X., Chen, L., Wu, F.Y., Liu, J.L., 2011. Timing, scale and mechanism of the destruction of the North China Craton. Sci. China: Earth Sci. 54 (6), 789–797.

Zhu, R.X., Xu, Y.G., Zhu, G., Zhang, H.F., Xia, Q.K., Zheng, T.Y., 2012a. Destruction of the North China Craton. Sci. China: Earth Sci. 55 (10), 1565–1587.

Zhu, R.X., Yang, J.H., Wu, F.Y., 2012b. Timing of destruction of the North China Craton. Lithos 149, 51–60.

Zhu, Q.Q., Xie, G.Q., Jiang, Z.S., Sun, J.F., Li, W., 2014. Characteristics and in situ U-Pb dating of hydrothermal titanite by LA-ICPMS of the Jingshandian iron skarn deposit, Hubei Province. Acta Petrol. Sin. 30 (5), 1322–1338 (in Chinese with English abstract).

Zhu, R.X., Fan, H.R., Li, J.W., Meng, Q.R., Li, S.R., Zeng, Q.D., 2015. Decratonic gold deposits. Sci. China: Earth Sci. 58 (9), 1523–1537.

Zhu, Q.Q., Xie, G.Q., Mao, J.W., Hou, K.J., Sun, J.F., Jiang, Z.S., 2017. Formation of the Jinshandian Fe skarn ore field in the Edong district, Eastern China: constraints from U-Pb and $^{40}Ar/$ ^{39}Ar geochronology. Ore Geol. Rev. 86, 1–20.

Zong, X.D., 1978. Structural ore-controlling rules and prospecting directions of Laiwu iron deposits. Geol. Expl. 5, 9–16 (in Chinese).

Zong, X.D., Xu, J., Lu, T.Y., Fang, C.Z., 2010. Structural types, ore body styles and occurrence pattern of large, large-medium iron deposits in Kuangshan iron ore field, Shandong province. Contribut. Geol. Mineral Resour. Res. 25 (3), 234–240 (in Chinese with English abstract).

Zong, X.D., Li, W., Wang, J., Qiao, W., Zhang, J.F., Liu, J.T., 2012. Study on rich iron ore fore martin teel and the by-products of Cu and Co in Zhangjiawa iron deposit of Shandong province. Contribut. Geol. Mine. Resour. Res. 27 (1), 60–65 (in Chinese with English abstract).